Numerical investigation on the behaviour of the high-strength ring strengthened dowel connection under vertical load

Jiachen GUO[a], *Tak-Ming CHAN*[a,*]

[a] *Department of Civil and Environmental Engineering, The Hong Kong Polytechnic University, Hong Kong, China*

* *Corresponding author: tak-ming.chan@polyu.edu.hk*

Numerical investigation on the behaviour of the high-strength ring strengthened dowel connection under vertical load

Abstract

To improve the bearing resistance of individual pavement connections at joint surface, an innovative high-strength ring strengthened dowel connection was developed. A comprehensive finite element analysis (FEA) was then conducted to investigate the ultimate load of this novel connection and the compressive stress development of concrete. Parameters including the compressive strength of high-strength concrete (HSC), the thickness and the length of the high-strength ring were analysed. The FEA results indicated that the ultimate load of the dowel connection was enhanced as the thickness and compressive strength of the high-strength ring increased. Due to the expanded contact area created by the high-strength ring, compressive stress created in normal-strength concrete was reduced, thereby delaying the initiation of localised concrete crushing. Furthermore, since the crushing failure primarily concentrated at the joint surface, the length of the high-strength rings was optimised to 25 mm to fully utilise the excellent compressive behaviour of HSC. Finally, based on the obtained FEA data, analytical models were derived to predict the maximum compressive stress of concrete under the service limit state and the ultimate load of the dowel connection embedded into concrete under the ultimate limit state.

Keywords: high-strength ring strengthened dowel connection, ultimate load, compressive stress concentration, parametric analysis, analytical models.

1. Introduction

With the development of national economy and the expansion of metropolitan regions, the urban traffic volume has witnessed a dramatic increase over the past two decades (Tayabji et al. 2013a, Tayabji et al. 2013b, Tomek 2017, Vaitkus et al. 2021). Therefore, current highway and urban road systems tend to suffer premature damages within their service life and require urgent maintenance (Tayabji et al. 2013a, Smith and Snyder 2019, Syed and Sonparote 2020a, Syed and Sonparote 2020b, Yaqoob et al. 2021). As one of the most widely used rigid

pavement systems, jointed plain concrete pavement (JPCP) systems are always applied in existing pavement rehabilitation as well as new pavement construction. To alleviate the internal stress caused by concrete shrinkage and expansion, JPCP systems are constructed with contraction and expansion joints. Epoxy-coated dowel bars are then installed along pavement joints at a spacing of 300 mm to improve the continuity of the whole pavement system (AASHTO 1993, ACI Committee 325 2002, Tayabji et al. 2013a, Tayabji et al. 2013b, Smith and Snyder 2019, Fang et al. 2022).

Figure 1 introduces the dowel bar load transfer mechanism which is achieved through the shear deformation of dowel bars and the bearing stress offered by surrounding concrete (Guo and Chan 2022a). However, despite of the effective load transfer between pavement slabs, the induced high bearing stress may lead to severe compressive stress concentration, thereby causing localised concrete crushing at the pavement joint surface (Riad et al. 2009, Al-Humeidawi and Mandal 2014b, Mackiewicz 2015a, Priddy et al. 2015, Mackiewicz and Szydło 2020). To investigate the mechanical behaviour of the dowel connection embedded into concrete under vertical load, Timoshenko's infinite beam on Winkler foundation model is adopted. The dowel connection is modelled by an elastic beam and the concrete support is simulated by the Winkler foundation (Timoshenko and Lessells 1925, Friberg et al. 1939, Shoukry et al. 2002, Zhang et al. 2022). As a result, the maximum compressive stress of concrete at the joint surface σ_0 can be derived by Equations (1) to (4) (Friberg et al. 1939), where, β refers to the modulus of dowel support of surrounding concrete (in N/mm^3); d is the dowel connection diameter (in mm); E and I are the modulus of elasticity (in N/mm^2) and the moment of inertia of the dowel connection (in mm^4), respectively; y_0 represents the maximum deformation of the concrete dowel slot at the joint surface; Δ_r denotes the relative deflection between pavement slabs (in mm); δ represents the shear deflection equal to $\lambda P_t z/AG$ (in mm); λ is the circular shape factor equal to 10/9; P_t is the transferred shear force (in kN); z is the

pavement joint width (in mm); *A* refers to the cross-section area of the dowel connection (in mm^2); *G* is the shear modulus (in N/mm^2).

$$\beta = \sqrt[4]{\frac{k_0 d}{4EI}} \quad (1)$$

$$y_0 = \frac{(\Delta_r - \delta)}{2} \quad (2)$$

$$y_0 = \frac{P_t}{4\beta^3 EI}(2 + \beta z) \quad (3)$$

$$\sigma_0 = k_0 y_0 \quad (4)$$

[Figure 1 is near here]

Apart from the analytical approach, finite element analysis (FEA) is also an effective approach to investigate the structural performance of a dowel connection embedded into concrete under vertical load. Existing modelling techniques are generally developed based on different types of finite element models.

For two-dimensional models, the following three modelling techniques have been proposed.

- Bending beams and two-dimensional plate elements are adopted to model dowel connections and concrete pavements, respectively. Contact elements are used between dowel connections and concrete to simulate the interaction between these two components (Zaman and Alvappillai 1995).
- Two-dimensional plate elements are used to simulate concrete pavements. A series of discrete spring elements are set between pavement slabs to model the pavement load transfer (Huang and Wang 1973, Huang 1985, Mahboub et al. 2004).
- Two-dimensional plate elements and beam elements are used to simulate concrete pavements and dowel bars, respectively. The interaction between concrete and dowel bars

is characterised by separate vertical spring elements with the support stiffness equal to the modulus of dowel support (Tabatabaie and Barenberg 1978, Guo et al. 1995, Zaman and Alvappillai 1995).

In terms of three-dimensional finite element models, the following two typical modelling techniques have been widely used by numerous researchers.

- Concrete pavement slabs and discrete dowel bars are modelled by three-dimensional solid elements and beam elements, respectively. The characteristics of the dowel-concrete interaction is simulated by vertical spring elements (Channakeshava et al. 1993, Kuo et al. 1995, Davids et al. 2003, Kim and Hjelmstad 2003, Maitra et al. 2009).
- Concrete pavement slabs and dowel bars are simulated by three-dimensional solid elements. The surface-to-surface contact modelling approach is used to model the interaction between dowel bars and concrete (Shoukry et al. 2002, Prabhu et al. 2009, Al-Humeidawi and Mandal 2014a, Mackiewicz 2015b, Priddy et al. 2015, Mackiewicz and Szydło 2020, Al-Humeidawi and Mandal 2022, Guo and Chan 2022a, Guo and Chan 2022c).

Among these modelling methods, the three-dimensional modelling technique together with the surface-to-surface contact simulation is proved to be the most accurate in the simulation of dowel-concrete interaction behaviour. Both the compressive stress concentration and localised concrete crushing at the joint surface can be well simulated as shown in Figure 2.

[Figure 2 is near here]

Compared with normal strength concrete (NSC), high-strength concrete (HSC) and ultra-high performance concrete (UHPC) exhibit superior compressive strength, stiffness, toughness, durability and low permeability (Ferraris et al. 2001, Shi et al. 2015, Zhou et al. 2018, Xu et al. 2022). Therefore, to improve the bearing resistance of the dowel connection embedded into

concrete, additional high-strength rings were applied to partially replace NSC around the dowel connection as shown in Figure 3 (Guo et al. 2023). Test results indicated that the incorporation of the high-strength ring greatly improved the bearing resistance of the dowel connection embedded into concrete under vertical load and delayed the occurrence of localised concrete crushing at the joint surface (Guo et al. 2023). Because of the superior compressive behaviour, in practical applications, the high-strength rings can be casted on individual dowel connections in factories and then cured in a controlled environment. Once HSC reaches the target compressive strength, dowel connections with the high-strength rings are transported to construction sites for existing pavement maintenance or new pavement construction.

[Figure 3 is near here]

However, as only a limited number of specimens were tested, the effects of different parameters on the structural behaviour of the high-strength ring strengthened dowel connection cannot be comprehensively investigated. In this paper, an extended parametric analysis was conducted through FEA following the existing test arrangement. Parameters including the compressive strength of HSC, the thickness and the length of the high-strength ring were studied. Based on test and FEA data, analytical models were proposed to predict the ultimate load of the dowel connection embedded into concrete under vertical load, and the maximum compressive stress created in concrete.

2. Finite element analysis

To investigate the structural performance of the high-strength ring strengthened dowel connection embedded into concrete, a comprehensive finite element analysis (FEA) was carried out via the general-purpose software ABAQUS 6.14 (ABAQUS 2014). Developed finite element models were validated against experimental test results in terms of the typical failure modes and the load-deflection curves. For analysing the concentrated compressive

stress generated in the high-strength ring and in the NSC concrete block, the global-local FEA was considered through the ABAQUS sub-modelling technique. Then an extended parametric analysis was carried out, and analytical models were derived according to the data obtained from the global and local FEA.

2.1.Finite element model

2.1.1. Model configuration

The finite element model was developed based on the test arrangement of the high-strength ring strengthened dowel connection embedded into concrete as shown in Figure 4. Due to the complexity of the test setup, the finite element model was simplified in terms of the modelling of components and the assignment of boundary conditions to minimise convergent issues. The configuration of the finite model is shown in Figure 5(a), which includes the dowel connection, the V-shape support device, the high-strength ring and the NSC block. Dimensions of components were the same as those in experimental tests as introduced in Figure 5(b). Considering the symmetric features of the test setup, only a half model was established to reduce the computational effort. The joint width between the V-shape support device and the joint surface was the same as that in experimental tests and equal to 10 mm.

[Figure 4 is near here]

[Figure 5 is near here]

2.1.2. Element and mesh size

Apart from the rigid V-shape support, all components in FEA were deformable and modelled by three-dimensional eight-node solid elements with reduced integration (C3D8R). After conducting the mesh sensitivity analysis, the minimum mesh size selected for the high-strength ring and the dowel connection was 3 mm to capture typical failure modes and

deformations. For the concrete block, the refined mesh with a size of 3 mm was assigned to the part of the block near the joint surface to reproduce the localised concrete crushing failure. However, because the part of the block away from the joint had a limited influence on the deflection response of the dowel connection, 6 mm-sized elements were adopted in this region to minimise the total number of elements and reduce the computational time.

2.1.3. Contact simulation and boundary conditions

In FEA, both the normal and the tangential contact behaviour were defined. For the normal contact behaviour, it was defined with the "hard contact" formulation without penetration allowed after contact. While for the tangential behaviour, it was modelled by the "penalty friction" formulation with the frictional coefficient equal to 0.35 (Al-Humeidawi and Mandal 2022). The interaction between the high-strength ring and the NSC concrete block was modelled by a tie constraint to prevent the separation of these two parts. In terms of boundary conditions, a symmetric constraint was firstly established along *z* axis as shown in Figure 6(a). Then for the rigid V-shape support device, as displayed in Figure 6(b), all degrees of freedom of the referenced point were restrained to provide the reaction force. Figure 6(c) introduces the displacement-type vertical load applied to the concrete block through the reference point RP-1 at a distance of 25 mm from the joint surface.

[Figure 6 is near here]

2.2.Materials

2.2.1. Normal-strength concrete (NSC)

The concrete damaged plasticity (CDP) model available in ABAQUS was used to simulate the compressive and tensile behaviour of NSC (Lubliner et al. 1989, Lee and Fenves 1998). In the CDP model, the uniaxial compressive and tensile behaviour of concrete were firstly defined. For the uniaxial compressive behaviour, a linear stress-strain relationship was defined before

$0.4f_c$ and followed by a nonlinear stage as expressed by Equations (5) to (7) proposed in CEB-FIP Model code for concrete structures (2010), where f_c is the cylinder compressive strength; σ_c is the compressive stress; ε_c is the compressive strain; ε_{cl} is the compressive strain at the maximum compressive stress; $\varepsilon_{c,lim}$ is the limited compressive strain at $0.5f_c$ within the descending stage; E_{ci} is the tangential modulus of elasticity at the origin; E_{cl} is the secant modulus of elasticity at the cylinder compressive strength; k is the plasticity number equal to E_{ci}/E_{cl}. Regarding the descending stage beyond the range of Equation (5), the stress-strain relationship proposed in CEB-FIP Model code 1990 (1993) was adopted as indicated in Equations (8) and (9). The required material parameters were acquired through the uniaxial compression test as summarised in Table 1, in which E_c is the secant modulus of elasticity at $0.4f_c$.

$$\frac{\sigma_c}{f_c} = \left[\frac{k\eta-\eta^2}{1+(k-2)\eta}\right] \ (\varepsilon_c \le \varepsilon_{c,lim}) \tag{5}$$

$$\eta = \left(\frac{\varepsilon_c}{\varepsilon_{cl}}\right) \tag{6}$$

$$k = \left(\frac{E_{ci}}{E_{cl}}\right) \tag{7}$$

$$\sigma_c = \left[\left(\frac{1}{\frac{\varepsilon_{c,lim}}{\varepsilon_{cl}}}\xi - \frac{2}{(\frac{\varepsilon_{c,lim}}{\varepsilon_{cl}})^2}\right)\left(\frac{\varepsilon_c}{\varepsilon_{cl}}\right)^2 + \left(\frac{4}{\frac{\varepsilon_{c,lim}}{\varepsilon_{cl}}} - \xi\right)\left(\frac{\varepsilon_c}{\varepsilon_{cl}}\right)\right]^{-1} f_c \ (\varepsilon_c > \varepsilon_{c,lim}) \tag{8}$$

$$\xi = \frac{4\left[(\frac{\varepsilon_{c,lim}}{\varepsilon_{cl}})^2\left(\frac{E_{ci}}{E_{cl}}-2\right)+2\frac{\varepsilon_{c,lim}}{\varepsilon_{cl}}-\frac{E_{ci}}{E_{cl}}\right]}{\left[\frac{\varepsilon_{c,lim}}{\varepsilon_{cl}}\left(\frac{E_{ci}}{E_{cl}}-2\right)+1\right]^2} \tag{9}$$

[Table 1 is near here]

As the tensile stress-strain relationship was sensitive to the mesh size, it was recommended to use the mesh-independent stress-crack width relationship to describe the uniaxial tensile behaviour of concrete. Therefore, the tensile stress-crack width curve proposed in CEB-FIP

Model code for concrete structures (2010) was used as expressed by Equations (10) to (14), where, σ_{ct} and f_t refer to tensile stress and the splitting tensile strength of concrete, respectively; w, w_t and w_c represent the crack width, the transition crack width and the crack opening width, respectively; G_F denotes the concrete fracture energy. After obtaining the splitting tensile strength f_t, related parameters were determined as listed in Table 2.

$$\sigma_{ct} = f_t\left(1.0 - 0.8\frac{w}{w_1}\right) \ (w \le w_t) \tag{10}$$

$$\sigma_{ct} = f_t\left(0.25 - 0.05\frac{w}{w_1}\right) \ (w_t < w \le w_c) \tag{11}$$

$$G_F = 0.73(f_c)^{0.18} \tag{12}$$

$$w_t = \frac{G_F}{f_t} \tag{13}$$

$$w_c = \frac{5G_F}{f_t} \tag{14}$$

[Table 2 is near here]

In order to account for the effects of concrete crushing and tensile cracks on the stiffness reduction, the concrete damage variables were considered in FEA. The definition of the concrete damage variable was explained in Figure 7. As the concrete plastic deformation increased, the modulus of elasticity of concrete was impaired and expressed by $E_c(1\text{-}D)$, where D represented the compressive or tensile damage variable that was increased with accumulative plastic deformation. The range of the concrete damage variable was from zero to one, representing no damage and complete damage, respectively. For the compressive damage variable D_c, it was defined from the compressive stress σ_c, the plastic strain ε_c^{pl} and the inelastic strain ε_c^{in} as indicated in Equations (15) and (16). Then for the tensile damage variable D_t, this parameter increased as cracks propagated and was proportional to the

dissipated energy in forming cracks. Thus, Equations (17) and (18) were derived to compute D_t at crack width w.

$$D_c = 1 - \frac{\sigma_c E_c^{-1}}{(\varepsilon_c^{in} - \varepsilon_c^{pl}) + \sigma_c E_c^{-1}} \quad (15)$$

$$\varepsilon_c^{pl} = 0.7\varepsilon_c^{in} \quad (16)$$

$$D_t = \frac{f_t\left(w - 0.4\frac{w^2}{w_t}\right)}{G_F} \ (w \le w_t) \quad (17)$$

$$D_t = 1 - \frac{\left[f_t\left(0.125 - 0.025\frac{w}{w_t}\right)(w_c - w)\right]}{G_F} \ (w_t < w \le w_c) \quad (18)$$

Other required parameters in the CDP model including the dilation angle ψ, the biaxial stress ratio f_{b0}/f_c, the tensile meridian to the compressive meridian ratio K, the eccentricity ε and the viscosity parameter were obtained from the ABAQUS user's guide (2014) and the recommendation provided by Al-Humeidawi and Mandal (2022), equal to 30˚, 1.16, 0.667, 0.1 as well as zero, respectively.

[Figure 7 is near here]

2.2.2. High-strength concrete

In FEA, three types of HSC labelled by Ring-0.2, Ring-0.3 and Ring-0.4 with water-to-binder ratios of 0.2, 0.3 and 0.4 were used to fabricate high-strength rings. The definition of the compressive behaviour of HSC was similar to that of NSC. The ascending stage of the compressive stress-strain relationship was defined based on the obtained material test data. While for the descending stage, Equations (5) to (9) were also adopted to define the uniaxial compressive stress-strain relationship. The material properties of HSC are summarised in Table 3. Due to the linear stress-strain behaviour, the modulus of elasticity E_c of Ring-0.2 and Ring-0.3 were determined at $0.7f_c$ instead of $0.4f_c$ to better fit the material test data.

[Table 3 is near here]

Regarding the uniaxial tensile behaviour of the HSC, as there was no fibre included in the mix proportions of HSC, the stress-crack width relationship expressed by Equations (10) to (14) was applied. Table 4 summarises the material parameters of HSC under uniaxial tension. The compressive stress-strain relationships and the tensile stress-crack width curves of NSC and HSC are plotted in Figure 8 and Figure 9, respectively. Corresponding compressive and tensile damage variables were then determined by Equations (15) to (18). Other plasticity parameters for defining HSC in the CDP model were the same as those adopted in the simulation of NSC.

[Table 4 is near here]

[Figure 8, 9 are near here]

2.2.3. Steel

The material properties of the 16 mm and 19 mm dowel connections were acquired by conducting uniaxial tension tests as shown in Figure 10(a) (Guo et al. 2023). Figure 10(b) plots the obtained nominal stress-strain curves of dowel connections. The true stress-strain relationships were then obtained via the converted equations as expressed by Equations (19) and (20), where ε_n and σ_n represent the normal strain and normal stress, respectively; ε_t and σ_t indicate the true strain and true stress, respectively.

$$\sigma_t = \sigma_n(1 + \varepsilon_n) \tag{19}$$

$$\varepsilon_t = \ln(1 + \varepsilon_n) \tag{20}$$

[Figure 10 is near here]

2.3.Model validation

After developing the finite element model of the high-strength ring strengthened dowel connection embedded into concrete, FEA was conducted via the ABAQUS explicit solver which was preferred in the analysis of complex structures to avoid convergent issues. To reduce the computational effort, a mass scaling factor (MSF) was incorporated to expand the weight of elements and increase the critical time increment. After comparing the kinetic energy (ALLKE) and internal energy (ALLIE) generated from the history output, the target time increment was adjusted to 10^{-5} to ensure the quasi-static analysis (Debnath and Chan 2021).

In FEA, each model was labelled by the dowel connection diameter, the thickness and length of the high-strength ring and the water-to-binder ratio (*w/b*) of HSC sequentially. Developed models were firstly validated against the test data in terms of failure modes. Both localised concrete crushing and horizontal tensile cracks were observed at the pavement joint surface as stressed by red lines and yellow lines in Figure 11. These typical failure modes can be precisely simulated by the compressive and tensile damage variables of concrete, respectively. Table 5 compares the size of concrete crushing zone predicted in FEA with that measured in experimental tests. In spite of a slight deviation, the range of this critical region can be accurately simulated with a mean value of 1.02 and coefficient of variation (CoV) of 0.08.

[Figure 11 is near here]

[Table 5 is near here]

Apart from failure modes, the load-deflection curves generated from FEA also matched those recorded in experimental tests as displayed in Figure 12. Table 6, Table 7 and Figure 13 compare the ultimate loads of specimens obtained from experimental tests and generated from

FEA. Close agreements are achieved with mean values of 1.02 and 1.01, and coefficients of variation (CoV) of 0.020 and 0.011.

[Figures 12, 13 are near here]

[Tables 6 and 7 are near here]

2.4.Local finite element analysis

Although validated FE models were accurate in predicting the ultimate load and the deflection response of each model, compressive stress concentration observed in the high-strength ring and the NSC concrete block was difficult to be analysed due to the relatively coarse mesh. Therefore, the most effective approach to minimise the computational effort and focus on the localised stress state without losing the fidelity of the solution was to conduct the global-local analysis (Reinoso et al. 2012, Hühne et al. 2016, Nagaraj et al. 2021). In ABAQUS, the global-local analysis was implemented by using the sub-modelling technique which was achieved via two steps as introduced in Figure 14 (ABAQUS 2014). Firstly, the global model was developed and then validated against experimental test results. Then the solutions of the global model were adopted as the boundary conditions of the local model including the critical zone. To ensure the convergent compressive stress, the size of the refined mesh was adjusted to 1 mm along the radial direction of the high-strength ring after implementing the mesh sensitivity analysis. Choosing the model 19-10-50-0.2 as an example, as shown in Figure 15, the convergent compressive stress produced in the local model was almost double that of the global model. This revealed that the localised compressive stress generated in the global model was not reliable and should not be adopted in the compressive stress prediction.

[Figure 14, 15 are near here]

3. Parametric analysis

Both global and local models were developed to comprehensively analyse the effects of the compressive strength of HSC, the high-strength ring thickness and length on the structural behaviour of a dowel connection embedded into concrete under the service limit state (SLS) and the ultimate limit state (ULS), respectively.

3.1.Compressive strength of high-strength concrete

Due to the superior bearing resistance, the application of the high-strength rings considerably mitigated localised concrete crushing at the joint surface and improved the ultimate load of a dowel connection embedded into concrete. Figure 16 plots the deflection response of the models with 16 mm and 19 mm dowel connections and strengthened by 10 mm-thick high-strength rings. It was found that the high-strength rings enhanced both the ultimate load and the initial stiffness. This effect became more pronounced as the compressive strength of HSC increased. Based on the beam on elastic foundation (BEF) theory, the range of the concrete compressive zone near the joint surface was reduced with the increased concrete support stiffness (Guo and Chan 2022b). As a result, as seen in Figure 17, the high-strength rings made of HSC with higher compressive strength experienced a faster compressive stress development as the vertical load increased. Under the service limit state (SLS), the allowable load of the high-strength ring strengthened dowel connection embedded into concrete was specified when the compressive strength of HSC or NSC was reached. Using models 16-5-50 and 19-7.5-50 as examples, Figure 18 plots the maximum compressive stress development in the high-strength ring and the NSC block, respectively. As can be seen from the dash lines, the compressive strength of HSC had a limited impact on the stress development of the NSC block. Table 8 summarises the allowable load of the developed models and the generated compressive stress in the high-strength ring and in the NSC block. As the compressive

strength of HSC increased, the locations of concrete crushing initiation shifted from the NSC block to the high-strength ring.

[Figures 16 to 18 are near here]

[Table 8 is near here]

3.2.High-strength ring thickness

The thickness of the high-strength ring is a critical parameter influencing the allowable load and the ultimate load of a dowel connection embedded into concrete and affecting the compressive stress development in the high-strength ring and the NSC block. Figure 19 shows the deflection response of models with high-strength rings of varying thicknesses. Although increasing the ring thickness improved the ultimate load, the effect on the ultimate load was no longer significant when the effective thickness t_{eff} was reached. At this point, localised crushing in the NSC block was less developed. As introduced in Figure 20, the effective thicknesses of models 16-0.4 and 19-0.4 were 15 mm and 17.5 mm, respectively. And the effective thicknesses of models 16-0.2(0.3) and 19-0.2(0.3) were 17.5 mm and 22.5 mm, respectively.

Additionally, increasing the thickness of the high-strength ring expanded the interface between the NSC block and the ring part, thus resulting in a reduced compressive stress development in NSC as plotted in Figure 21. Based on the data summarised in Table 9 to Table 14, the thickness of the high-strength ring affected both the allowable load under the service limit state (SLS) and the location of concrete crushing initiation. As the ring thickness increased, the location of crushing initiation was transferred from the NSC concrete block to the high-strength ring.

[Figures 19 to 21 are near here]

[Tables 9 to 14 are near here]

3.3.High-strength ring length

In accordance with the BEF theory, the compressive stress created in the dowel slot decreased with the increase of the longitudinal distance between the contact point and the joint surface. Therefore, under vertical load, severe concrete crushing primarily concentrated at a limited zone close to the joint surface. Figure 22 plots the load-deflection relationships of models with the high-strength rings of different lengths. As the ring length increased, the region strengthened by the high-strength ring was expanded. Therefore, the bearing resistance of the dowel connection embedded into concrete under vertical load was enhanced and a higher ultimate load was thus generated. However, as shown in Figure 23, the effect of the ring length on the load improvement became insignificant when the ring length exceeded 25 mm. This revealed that, for dowel connections with diameters of 16 mm and 19 mm, the depth of the localised concrete crushing zone was smaller than 25 mm as the vertical load increased.

[Figures 22 and 23 are near here]

4. Assessments of parameters

Through the comprehensive parametric analysis, the effects of critical parameters including the compressive strength of HSC, the thickness and the length of the high-strength ring on the structural behaviour of a dowel connection embedded into concrete have been thoroughly investigated. Due to the concentrated compressive stress induced at the pavement joint surface, the allowable load and the ultimate load of a dowel connection embedded into concrete are primarily affected by the compressive strength of HSC. Regarding the high-strength ring thickness, the contact area between the ring part and the NSC concrete block expands as the thickness increases. As a result, the maximum compressive stress generated in the NSC is reduced and the ultimate load of the model is thus improved. In terms of the high-

strength ring length, this parameter primarily influences the regions reinforced by the high-strength rings. As localised crushing failure only occurs near the pavement joint surface, according to the FEA data, the high-strength rings with a length of at least 25 mm are recommended to make full use of the excellent compressive behaviour of HSC.

5. Analytical models of the high-strength ring strengthened dowel connection

Dowel connections installed along transverse joints of concrete pavement take varying vertical loads at different locations. The most critical dowel connection is positioned just under the wheel and transfers the highest vertical load to the adjacent pavement slab. As a result, it is essential to analyse the capacity of each dowel connection under vertical load to prevent premature joint failure. Additionally, each dowel connection needs to sustain millions of load repetitions within the pavement service life. As a result, it is crucial to avoid the occurrence of localised concrete crushing around the dowel connection. In section 5.1, an analytical model is derived to predict the ultimate load of the high-strength ring strengthened dowel connection embedded into concrete under vertical load. While in section 5.2, a relationship is established between the maximum compressive stresses produced in the normal-strength concrete block and the high-strength ring under the service limit state.

5.1. Ultimate load prediction`

Based on the experimental test setup, the force diagram of a dowel connection embedded into concrete is shown in Figure 24. The force transferred by an individual dowel connection at each side was equal to P_t. Under the ultimate limit state (ULS), a plastic hinge formed in the dowel connection and localised concrete crushing occurred at the joint surface (Rasmussen 1963, Soroushian et al. 1987, CEB-FIP 2010, Randl 2013, Jeong et al. 2020, Zhao et al. 2021).

To determine the maximum shear force transferred by the dowel connection $V_{F,max}$, the force and moment equilibriums are derived as expressed by Equations (21) to (23), where, M_{pl} is the plastic moment resistance of the dowel connection; f_y represents the yield strength of steel; d is the diameter of the dowel connection; l_0 refers to the distance between the plastic hinge and the joint surface; z is the joint width between the V-shape support device and the joint surface; β_c denotes the stress improvement factor considering the confined compressive strength of concrete. By solving the force and moment equilibriums, the maximum shear force transferred by an individual dowel connection is acquired as expressed by Equations (24) to (26). After fitting to experimental test results, the stress improvement factors for models with 16 mm and 19 mm dowel connections are equal to 4.3 and 3.1, respectively, which is within the range of 3 to 5 times the cylinder compressive strength of concrete recommended by Rasmussen (1963).

$$V_{F,max} = P_t = l_0 d \beta_c f_c \tag{21}$$

$$M_{pl} = \frac{f_y d^3}{6} \tag{22}$$

$$M_{pl} = P_t z + P_t^2/(2\beta_c f_c d) \tag{23}$$

$$V_{F,max} = k_d A_s \sqrt{f_y f_c} \tag{24}$$

$$k_d = \frac{4}{\pi}\left(\sqrt{\beta_c^2 \alpha^2 + \frac{1}{3}\beta_c} - \beta_c \alpha\right) \tag{25}$$

$$\alpha = \frac{z}{d}\sqrt{\frac{f_c}{f_y}} \tag{26}$$

[Figure 24 is near here]

Furthermore, as discussed in the parametric analysis section, the ultimate load of the high-strength ring strengthened dowel connection embedded into concrete closely depends on the compressive strength of HSC and the thickness of the high-strength ring. According to

Equation (24), the maximum shear force transferred by an individual connection is proportional to the square root of the cylinder compressive strength of concrete. As a result, a non-dimensional parameter $\sqrt{\frac{f_{c,ring}}{f_c}}\frac{t}{d}$ is proposed to evaluate the effects of these two parameters on improving the ultimate load, where, $f_{c,ring}$ and f_c are the cylinder compressive strengths of HSC and NSC, respectively; t is the thickness of the high-strength ring. Then with the application of the test and the FEA data, a close linear relationship is observed between the load ratio $N_{u,ring}/N_{u,d}$ and the non-dimensional parameter $\sqrt{\frac{f_{c,ring}}{f_c}}\frac{t}{d}$ as shown in Figure 25, where $N_{u,ring}$ and $N_{u,d}$ represent the ultimate loads of the specimens strengthened by the high-strength rings and that only with dowel connections, respectively. Therefore, the following Equation (27) is derived to predict the ultimate load of the high-strength ring strengthened dowel connection embedded into concrete under vertical load. Figure 26 and Table 15 to Table 17 compare the ultimate loads obtained from the FEA, experimental tests and the analytical prediction. Close agreements are achieved with the mean values of 0.99, 1.00 and the coefficient of variation (CoV) of 0.02.

$$\frac{N_{u,ring}}{N_{u,d}} = 0.288\sqrt{\frac{f_{c,ring}}{f_c}}\left(\frac{t}{d}\right) + 1 \quad (27)$$

In this section, the effects of the high-strength ring thickness and the compressive strength of HSC on the ultimate load of the dowel connection embedded into concrete are quantified with the FEA data. By applying a high-strength ring with a compressive strength of 145.4 MPa, the ultimate load of the dowel connection can increase by up to 65 percent. Increasing the high-strength ring thickness to 15 mm and 17.5 mm can also improve the ultimate load by 50 percent for 16 mm and 19 mm dowel connections, respectively.

[Figures 25 and 26 are near here]

[Tables 15 to 17 are near here]

5.2.Prediction of maximum compressive stress

By applying the high-strength ring, the contact area between the ring part and the NSC block was expanded, resulting in a reduction of the maximum compressive stress created in NSC. To optimise the design of the high-strength ring strengthened dowel connection, localised concrete crushing was intended to initiate in the high-strength ring and in the NSC block simultaneously. In the local FEA, before the initiation of concrete crushing, the maximum compressive stresses developed in the high-strength ring and in the NSC block are generated at the critical locations as displayed in Figure 27. The stress ratio λ is defined as the maximum compressive stress produced in the NSC block compared with that induced in the high-strength ring. The relationship between the stress ratio λ and the ring thickness t is plotted in Figure 28. It is noted that the stress ratio λ is not affected by the compressive strength of HSC while is closely dependent on the high-strength ring thickness. Consequently, a non-dimensional diameter ratio ($\frac{d}{d+2t}$) is proposed to account for the thickness effect, where (d+2t) refers to the external diameter of the high-strength ring. Figure 29 plots the relationship between the stress ratio λ and the diameter ratio ($\frac{d}{d+2t}$). According to the FEA data, the following Equation (28) is derived to predict the stress ratio λ considering the diameter of the dowel connection and the thickness of the high-strength ring. Figure 30, Table 18 and Table 19 compare the stress ratios determined based on the FEA data and predicted by the analytical solution. Close agreements are reached with the mean values of 1.00 and 0.97, and the coefficients of variation (CoV) of 0.04 and 0.05.

$$\lambda = \frac{\sigma_{\mathrm{NSC}}}{\sigma_{\mathrm{Ring}}} = \left(\frac{d}{d+2t}\right)^{2.16} \quad (28)$$

After identifying the compressive strength of NSC and HSC, the thickness of the high-strength ring can be optimised by Equation (28). For dowel connections with a diameter of 16 mm, the recommended high-strength ring thicknesses are 4 mm, 6 mm and 8 mm corresponding to HSC compressive strengths of 83.2 MPa, 117.2 MPa and 145.4 MPa, respectively. This ensures that the maximum compressive stresses developed in NSC and HSC will reach their compressive strengths simultaneously as the vertical load increases. Similarly, the corresponding high-strength ring thicknesses for dowel connections with a diameter of 19 mm are 5 mm, 7.5 mm and 9 mm, respectively.

[Figures 27 to 30 are near here]

[Tables 18 and 19 are near here]

6. Conclusions

In this paper, a comprehensive finite element analysis was carried out to investigate the mechanical behaviour of the high-strength ring strengthened dowel connection embedded into concrete under vertical load. The compressive strength of HSC, the thickness and the length of the high-strength ring were comprehensively investigated under both the service limit state and the ultimate limit state. The following conclusions are drawn based on the parametric analysis results:

1. The ultimate load of a dowel connection embedded into concrete enhances as the compressive strength of HSC increases. For dowel connections with a diameter of 16 mm or 19 mm, applying a high-strength ring with a compressive strength of 145.4 MPa can achieve a 65 percent ultimate load improvement.

2. The thickness of the high-strength ring is a critical parameter that influences the ultimate load of a dowel connection embedded into concrete. For dowel connections with a diameter of 16 mm, applying a high-strength ring of 15 mm thickness increases the

ultimate load by 50 percent. While for 19 mm dowel connections, the required high-strength ring thickness is 17.5 mm to result in a 50 percent ultimate load increase.

3. As the thickness of the high-strength ring increases, the contact area between the ring component and the NSC block expands, resulting in low compressive stress developed in NSC. As a result, the allowable load of the dowel connection embedded into concrete increases to delay the occurrence of localised concrete crushing at the joint surface. Applying a high-strength ring of 15 mm thickness can improve the allowable load by 120 percent for dowel connections with a diameter of 16 mm or 19 mm.

4. To improve the bearing resistance of a dowel connection embedded into concrete, the high-strength rings with a minimum length of 25 mm are suggested for the dowel connections with a diameter of 16 mm or 19 mm to maximise their excellent compressive behaviour.

5. For instructing the design of the high-strength ring strengthened dowel connection embedded into concrete, an analytical solution to predict the ultimate load of the dowel connection embedded into concrete under vertical load is derived and verified.

6. In order to prevent the occurrence of localised concrete crushing under the service limit state, the relationship between the maximum compressive stresses generated in the high-strength ring and in the NSC block is established. By optimising the thickness of the high-strength ring, the maximum compressive stresses in NSC and HSC will reach their compressive strengths simultaneously as the vertical load increases.

However, although this paper has quantified the effect of the high-strength ring on the structural performance of the dowel connection embedded into concrete, there are some future research needs to be carried out. Firstly, because dowel connections are subjected to repeated loads within pavement service life, it is necessary to conduct cyclic loading tests on the high-

strength ring strengthened dowel connection to assess its fatigue performance. Secondly, onsite field tests are also required for further evaluating the proposed high-strength ring strengthened connection. Dowel connections equipped with high-strength rings are fabricated in factories as commercially available products. During the onsite installation, the construction-related issues can be identified and then addressed to promote the practical application of this novel dowel connection.

Acknowledgements

The research work presented in this paper was supported by a grant from the Research Grants Council of the Hong Kong Special Administrative Region, China (Project no. R5007-18). Authors would like to sincerely acknowledge the advice on the joint design from Professor Yuhong Wang at The Hong Kong Polytechnic University.

Disclosure statement

No potential conflict of interest was reported by the author(s).

Funding

This work was supported by Research Grants Council, University Grants Committee [Grant number R5007-18].

References

American Association of State Highway and Transportation Officials, 1993. Guide for design of pavement structure. Washington D.C: AASHTO.

ABAQUS 6.14, 2014. Dassault systems, Waltham, MA, USA.

ABAQUS 6.14 CAE User's Guide, 2014. Dassault systems, Waltham, MA, USA.

ACI Committee 325, 2002. ACI 325.12R-02 Guide for design of jointed concrete pavements for streets and local roads. American Concrete Institute, Detroit, MI.

Al-Humeidawi, B. and Mandal, P., 2014a. Evaluation of performance and design of GFRP dowels in jointed plain concrete pavement–part 2: numerical simulation and design considerations. *International Journal of Pavement Engineering,* 15(8), 752-765.

Al-Humeidawi, B. H. and Mandal, P., 2014b. Evaluation of performance and design of GFRP dowels in jointed plain concrete pavement–part 1: experimental investigation. *International Journal of Pavement Engineering,* 15(5), 449-459.

Al-Humeidawi, B. H. and Mandal, P., 2022. Numerical evaluation of the combined effect of dowel misalignment and wheel load on dowel bars performance in JPCP. *Engineering Structures,* 252, 113655.

Channakeshava, C., Barzegar, F. and Voyiadjis, G. Z., 1993. Nonlinear FE analysis of plain concrete pavements with doweled joints. *Journal of Transportation Engineering,* 119(5), 763-781.

CEB/FIP, 1993. CEB-FIP model code 1990: Design code.Switzerland: Thomas Telford Publishing.

CEB/FIP, 2010. Model code for concrete structures. Berlin, Germany: Ernst & Sohn, Wiley.

Davids, W. G.*, et al.*, 2003. Three-dimensional finite element analysis of jointed plain concrete pavement with EverFE2.2. *Transportation Research Record,* 1853(1), 92-99.

Debnath, P. P. and Chan, T.-M., 2021. A comprehensive numerical approach for modelling blind-bolted CFST connections. *Structures,* 33, 2208-2225.

Fang, M. J., et al. 2022. Precast system and assembly connection of cement concrete slabs for road pavement: A review. Journal of Traffic and Transportation Engineering-English Edition, 9(2), 208-222.

Ferraris, C. F., Obla, K. H. and Hill, R., 2001. The influence of mineral admixtures on the rheology of cement paste and concrete. *Cement concrete research,* 31(2), 245-255.

Friberg, B., Richart, F. and Bradbury, R., 1939. Load and deflection characteristics of dowels in transverse joints of concrete pavements. *Highway Research Board Proceedings*.

Guo, H., Sherwood, J. A. and Snyder, M. B., 1995. Component dowel-bar model for load-transfer systems in PCC pavements. *Journal of Transportation Engineering,* 121(3), 289-298.

Guo, J.-C. and Chan, T.-M., 2022a. Stainless steel ring strengthened removable dowel bar connection system: Effect of key parameters and design recommendations. *Structures,* 44, 1767-1782.

Guo, J.-C. and Chan, T.-M., 2022b. Characteristics of compressive stress around dowel

joint in concrete pavement system. *International Journal of Pavement Engineering*.

Guo, J.-C. and Chan, T.-M., 2022c. Experimental and numerical study on the structural performance of the stainless steel ring strengthened removable dowel bar connection system. *International Journal of Pavement Engineering*.

Guo, J.-C., Chan, T.-M. and Wang, Y.-H., 2023. Experimental investigation on the structural performance of the high-strength ring strengthened dowel connection under monotonic load. *Engineering Structures,* 292, 116423.

Huang, Y., 1985. A computer package for structural analysis of concrete pavements. ed. *Third International Conference on Concrete Pavement Design and Rehabilitation*, Purdue University.

Huang, Y. and Wang, S., 1973. Finite-element analysis of concrete slabs and its implications for rigid pavement design. *Highway Research Record,* 466.

Hühne, S.*, et al.*, 2016. A two-way loose coupling procedure for investigating the buckling and damage behaviour of stiffened composite panels. *Composite Structures,* 136, 513-525.

Jeong, E.*, et al.*, 2020. Prediction of dowel action against concrete core without consideration of transverse reinforcement. *Journal of Structural Engineering,* 146(12), 04020279.

Kim, J. and Hjelmstad, K. D., 2003. Three-dimensional finite element analysis of doweled joints for airport pavements. *Transportation Research Record,* 1853(1), 100-109.

Kuo, C. M., Hall, K. T. and Darter, M. I., 1995. Three-dimensional finite element model

for analysis of concrete pavement support. *Transportation Research Record,* 1505.

Lee, J. and Fenves, G. L., 1998. Plastic-damage model for cyclic loading of concrete structures. *Journal of Engineering Mechanics,* 124(8), 892-900.

Lubliner, J.*, et al.*, 1989. A plastic-damage model for concrete. *International Journal of solids structures,* 25(3), 299-326.

Mackiewicz, P., 2015a. Analysis of stresses in concrete pavement under a dowel according to its diameter and load transfer efficiency. *Canadian Journal of Civil Engineering,* 42(11), 845-853.

Mackiewicz, P., 2015b. Finite-element analysis of stress concentration around dowel bars in jointed plain concrete pavement. *Journal of Transportation Engineering,* 141(6).

Mackiewicz, P. and Szydło, A., 2020. The analysis of stress concentration around dowel bars in concrete pavement. *Magazine of Concrete Research,* 72(2), 97-107.

Mahboub, K. C., Liu, Y. and Allen, D. L., 2004. Evaluation of temperature responses in concrete pavement. *Journal of Transportation Engineering,* 130(3), 395-401.

Maitra, S. R., Reddy, K. and Ramachandra, L., 2009. Load transfer characteristics of dowel bar system in jointed concrete pavement. *International Journal of Fracture,* 135(11), 813-821.

Nagaraj, M., Petrolo, M. and Carrera, E., 2021. A global–local approach for progressive damage analysis of fiber-reinforced composite laminates. *Thin-Walled Structures,* 169, 108343.

Prabhu, M., Varma, A. and Buch, N., 2009. Analytical investigation of the effects of dowel misalignment on concrete pavement joint opening behaviour. *International Journal of Pavement Engineering,* 10(1), 49-62.

Priddy, L. P.*, et al.*, 2015. Three-dimensional modelling of precast concrete pavement repair joints. *Magazine of Concrete Research,* 67(10), 513-522.

Randl, N., 2013. Design recommendations for interface shear transfer in fib Model Code 2010. *Structural Concrete,* 14(3), 230-241.

Rasmussen, B., 1963. The carrying capacity of tranceversely loaded bolts and dowels embedded in concrete. *Bygings Statiske Meddelser,* 34(2).

Reinoso, J.*, et al.*, 2012. Experimental and three-dimensional global-local finite element analysis of a composite component including degradation process at the interfaces. *Composites Part B: Engineering,* 43(4), 1929-1942.

Riad, M. Y.*, et al.*, 2009. Effect of skewed joints on the performance of jointed concrete pavement through 3D dynamic finite element analysis. *International Journal of Pavement Engineering,* 10(4), 251-263.

Shi, C.-J.*, et al.*, 2015. A review on ultra high performance concrete: Part I. Raw materials and mixture design. *Construction Building Materials,* 101, 741-751.

Shoukry, S. N., William, G. and Riad, M., 2002. Characteristics of concrete contact stresses in doweled transverse joints. *International Journal of Pavement Engineering,* 3(2), 117-129.

Smith, P. and Snyder, M. B., 2019. *Manual for Jointed Precast Concrete Pavement.* National Precast Concrete Association.

Soroushian, P., Obaseki, K. and Rojas, M. C., 1987. Bearing strength and stiffness of

concrete under reinforcing bars. *Materials Journal,* 84(3), 179-184.

Syed, A. and Sonparote, R. S., 2020a. A Review of Precast Concrete Pavement Technology. *Baltic Journal of Road Bridge Engineering,* 15(4), 22-53.

Syed, A. and Sonparote, R. S., 2020b. Construction of Pretensioned Precast Concrete Pavement. *Iranian Journal of Science and Technology-Transactions of Civil Engineering*, 44, 507-514.

Tabatabaie, A. M. and Barenberg, E., 1978. Finite-element analysis of jointed or cracked concrete pavements. *Transportation Research Record,* (671), 11-19.

Tayabji, S., Ye, D. and Buch, N., 2013a. Precast concrete pavement technology. *Transportation Research Board*.

Tayabji, S., Ye, D. and Buch, N., 2013b. Precast concrete pavements: Technology overview and technical considerations. *PCI Journal,* 58(1), 112-128.

Timoshenko, S. and Lessells, J. M., 1925. *Applied elasticity.* Westinghouse technical night school press.

Tomek, R., 2017. Advantages of precast concrete in highway infrastructure construction. *Procedia engineering,* 196, 176-180.

Vaitkus, A., Šernas, O. and Gražulytė, J., 2021. Modular pavements: Developing high performance concrete. *Construction Building Materials,* 292, 123362.

Xu, L.-Y*., et al.*, 2022. High-strength high-ductility Engineered/Strain-Hardening Cementitious Composites (ECC/SHCC) incorporating geopolymer fine aggregates. *Cement Concrete Composites,* 125, 104296.

Yaqoob, S., Silfwerbrand, J. and Strömberg, L., 2021. Evaluation of Rapid Repair of

Concrete Pavements Using Precast Concrete Technology: A Sustainable and Cost-Effective Solution. Nordic Concrete Research, 65(2), 107-128.

Zaman, M. and Alvappillai, A., 1995. Contact-element model for dynamic analysis of jointed concrete pavements. *Journal of Transportation Engineering,* 121(5), 425-433.

Zhang, J., *et al.*, 2022. Mechanical behavior of doweled joints in concrete pavements: A review. Journal of Transportation Engineering, Part B: Pavements, 148(4), 03122002.

Zhao, Y.*, et al.*, 2021. Experimental study of the shear behaviour of concrete-grout-concrete joints. *Journal of Building Engineering,* 43, 103095.

Zhou, M.*, et al.*, 2018. Application of ultra-high performance concrete in bridge engineering. *Construction Building Materials,* 186, 1256-1267.

Tables

Table 1 Material properties of normal-strength concrete (uniaxial compression).

f_c (MPa)	ε_{cl}	E_{ci} (GPa)	E_{cl} (GPa)	E_c (GPa)	k
34.45	0.0024	29.6	14.4	26.2	2.06

Table 2 Material properties of normal-strength concrete (uniaxial tension).

f_t (MPa)	G_F (N/mm)	w_t (mm)	w_c (mm)
3.49	0.138	0.0396	0.198

Table 3 Material properties of high-strength concrete (HSC) (uniaxial compression).

HSC	f_c (MPa)	ε_{cl}	E_{ci} (GPa)	E_{cl} (GPa)	E_c (GPa)	k
Ring-0.2	145.4	0.0044	39.2	33.2	35.2	1.18
Ring-0.3	117.2	0.0044	35.2	27.1	30.1	1.30
Ring-0.4	83.2	0.0046	30.5	18.3	28.2	1.67

Table 4 Material properties of high-strength concrete (HSC) (uniaxial tension).

HSC	f_t (MPa)	G_F (N/mm)	w_t (mm)	w_c (mm)
Ring-0.2	7.20	0.178	0.0247	0.124
Ring-0.3	6.38	0.171	0.0268	0.134
Ring-0.4	5.27	0.161	0.0306	0.153

Table 5 Comparison of the size of concrete crushing zone.

Model ID	S_{Test} (mm^2)	S_{FEA} (mm^2)	S_{Test}/S_{FEA}
16 mm	1247.7	1367.8	1.10
16-10-50-0.3	953.2	896.4	0.94
19 mm	1214.5	1276.2	1.05
19-10-50-0.3	821.3	897.2	1.09
19-15-50-0.2	1178.4	1075.7	0.91
		Mean	1.02
		CoV	0.08

Table 6 Ultimate load comparison between tests and FEA (16 mm).

Specimen ID	$N_{u,Test}$ (kN)	$N_{u,FE}$ (kN)	$N_{u,FE}/N_{u,Test}$
16 mm-1	89.9	89.60	1.00
16 mm-2	91.6	89.60	0.98
16-10-25-0.2-1	126.3	125.66	1.00
16-10-25-0.2-2	124.1	125.66	1.01
16-10-25-0.3-1	119.4	120.36	1.01
16-10-25-0.3-2	122.7	120.36	0.98
16-10-50-0.2-1	126.0	125.84	1.00
16-10-50-0.2-2	126.6	125.84	0.99
16-10-50-0.3-1	120.6	121.38	1.01
16-10-50-0.3-2	121.4	121.38	1.00
16-15-50-0.2-1	136.8	143.68	1.05
16-15-50-0.2-2	138.4	143.68	1.04

16-15-50-0.3-1	132.0	136.67	1.04
16-15-50-0.3-2	134.5	136.67	1.02
		Mean	1.01
		CoV	0.020

Table 7 Ultimate load comparison between tests and FEA (19 mm).

Specimen ID	$N_{u,Test}$ (kN)	$N_{u,FE}$ (kN)	$N_{u,FE}/N_{u,Test}$
19 mm-1	120.4	121.92	1.01
19 mm-2	120.2	121.92	1.01
19-10-50-0.2-1	155.1	158.63	1.02
19-10-50-0.2-2	155.9	158.63	1.02
19-10-50-0.3-1	152.1	155.52	1.02
19-10-50-0.3-2	155.9	155.52	1.00
19-15-50-0.2-1	173.6	180.84	1.04
19-15-50-0.2-2	176.6	180.84	1.02
		Mean	1.02
		CoV	0.011

Table 8 Maximum compressive stress and crushing initiation location under allowable load.

Model ID	$\sigma_{c,ring}$ (MPa)	$\sigma_{c,NSC}$ (MPa)	Allowable load (kN)	Crushing location
16-5-50-0.2	101.44	34.45	20.40	NSC block
16-5-50-0.3	100.06	34.45	20.48	NSC block
16-5-50-0.4	83.20	29.48	17.69	Ring
19-7.5-50-0.2	135.97	34.45	36.79	NSC block
19-7.5-50-0.3	117.20	30.67	32.69	Ring
19-7.5-50-0.4	83.20	22.69	24.09	Ring

Table 9 Maximum compressive stress and crushing initiation location under allowable load (16 mm-0.2).

Model ID	$\sigma_{c,ring}$ (MPa)	$\sigma_{c,NSC}$ (MPa)	Allowable load (kN)	Crushing location
16 mm	-	34.45	7.24	NSC block
16-2.5-50-0.2	64.75	34.45	13.05	NSC block
16-5-50-0.2	101.44	34.45	20.40	NSC block
16-7.5-50-0.2	145.40	33.63	25.73	Ring
16-10-50-0.2	145.40	24.44	25.38	Ring
16-12.5-50-0.2	145.40	18.71	25.18	Ring
16-15-50-0.2	145.40	14.63	24.95	Ring
16-17.5-50-0.2	145.40	11.91	24.80	Ring
16-20-50-0.2	145.40	9.66	24.74	Ring

Table 10 Maximum compressive stress and crushing initiation location under allowable load (16 mm-0.3).

Model ID	$\sigma_{c,ring}$ (MPa)	$\sigma_{c,NSC}$ (MPa)	Allowable load (kN)	Crushing location
16 mm	-	34.45	7.24	NSC block
16-2.5-50-0.3	66.17	34.45	13.18	NSC block
16-5-50-0.3	100.06	34.45	20.48	NSC block
16-7.5-50-0.3	117.20	28.63	21.57	Ring

16-10-50-0.3	117.20	19.20	21.43	Ring
16-12.5-50-0.3	117.20	14.60	21.30	Ring
16-15-50-0.3	117.20	12.24	21.23	Ring
16-17.5-50-0.3	117.20	9.72	21.17	Ring
16-20-50-0.3	117.20	8.07	21.10	Ring

Table 11 Maximum compressive stress and crushing initiation location under allowable load (16 mm-0.4).

Model ID	$\sigma_{c,ring}$ (MPa)	$\sigma_{c,NSC}$ (MPa)	Allowable load (kN)	Crushing location
16 mm	-	34.45	7.24	NSC block
16-2.5-50-0.4	69.23	34.45	13.59	NSC block
16-5-50-0.4	83.20	29.48	17.69	Ring
16-7.5-50-0.4	83.20	21.33	16.96	Ring
16-10-50-0.4	83.20	15.53	16.87	Ring
16-12.5-50-0.4	83.20	11.52	16.75	Ring
16-15-50-0.4	83.20	9.20	16.21	Ring
16-17.5-50-0.4	83.20	6.50	16.17	Ring
16-20-50-0.4	83.20	6.05	16.10	Ring

Table 12 Maximum compressive stress and crushing initiation location under allowable load (19 mm-0.2).

Model ID	$\sigma_{c,ring}$ (MPa)	$\sigma_{c,NSC}$ (MPa)	Allowable load (kN)	Crushing location
19 mm	-	34.45	10.42	NSC block
19-2.5-50-0.2	72.39	34.45	20.67	NSC block
19-5-50-0.2	100.40	34.45	29.15	NSC block
19-7.5-50-0.2	135.97	34.45	36.79	NSC block
19-10-50-0.2	145.40	29.65	38.69	Ring
19-12.5-50-0.2	145.40	23.18	37.13	Ring
19-15-50-0.2	145.40	18.95	36.04	Ring
19-17.5-50-0.2	145.40	15.58	35.39	Ring
19-20-50-0.2	145.40	13.11	35.17	Ring

Table 13 Maximum compressive stress and crushing initiation location under allowable load (19 mm-0.3).

Model ID	$\sigma_{c,ring}$ (MPa)	$\sigma_{c,NSC}$ (MPa)	Allowable load (kN)	Crushing location
19 mm	-	34.45	10.42	NSC block
19-2.5-50-0.3	71.76	34.45	20.70	NSC block
19-5-50-0.3	98.59	34.45	30.19	NSC block
19-7.5-50-0.3	117.20	30.67	32.69	Ring
19-10-50-0.3	117.20	25.38	31.55	Ring
19-12.5-50-0.3	117.20	18.81	30.34	Ring
19-15-50-0.3	117.20	15.60	29.92	Ring
19-17.5-50-0.3	117.20	12.88	29.55	Ring
19-20-50-0.3	117.20	10.85	29.42	Ring

Table 14 Maximum compressive stress and crushing initiation location under allowable load (19 mm-0.4).

Model ID	$\sigma_{c,ring}$ (MPa)	$\sigma_{c,NSC}$ (MPa)	Allowable load (kN)	Crushing location
19 mm	-	34.45	10.42	NSC block
19-2.5-50-0.4	67.82	34.45	21.06	NSC block
19-5-50-0.4	83.20	30.27	25.47	Ring
19-7.5-50-0.4	83.20	22.69	24.09	Ring
19-10-50-0.4	83.20	18.07	23.66	Ring
19-12.5-50-0.4	83.20	14.46	23.02	Ring
19-15-50-0.4	83.20	11.89	22.89	Ring
19-17.5-50-0.4	83.20	9.62	22.55	Ring
19-20-50-0.4	83.20	8.11	22.53	Ring

Table 15 Ultimate load comparison (Ring-0.2).

Specimen ID	$N_{u,Test(FE)}$	$\frac{t}{d}$	$\sqrt{\frac{f_{c,ring}}{f_c}}$	$\frac{t}{d}\sqrt{\frac{f_{c,ring}}{f_c}}$	$N_{u,Pred}$	$N_{u,Pred}/N_{u,Test(FE)}$
16-10-25-0.2-1	126.3	0.63	2.05	1.28	124.33	0.98
16-10-25-0.2-2	124.1	0.63	2.05	1.28	124.33	1.00
16-10-50-0.2-1	126.0	0.63	2.05	1.28	124.33	0.99
16-10-50-0.2-2	126.6	0.63	2.05	1.28	124.33	0.98
16-15-50-0.2-1	136.8	0.94	2.05	1.92	141.10	1.03
16-15-50-0.2-2	138.4	0.94	2.05	1.92	141.10	1.02
19-10-50-0.2-1	155.1	0.53	2.05	1.08	157.71	1.02
19-10-50-0.2-2	155.9	0.53	2.05	1.08	157.71	1.01
19-15-50-0.2-1	173.6	0.79	2.05	1.62	176.42	1.02
19-15-50-0.2-2	176.6	0.79	2.05	1.62	176.42	1.00
16-2.5-50-0.2	94.50	0.16	2.05	0.32	99.18	1.05
16-5-50-0.2	103.14	0.31	2.05	0.64	107.57	1.04
16-7.5-50-0.2	115.24	0.47	2.05	0.96	115.95	1.01
16-10-50-0.2	125.66	0.63	2.05	1.28	124.33	0.99
16-12.5-50-0.2	134.84	0.78	2.05	1.60	132.71	0.98
16-15-50-0.2	143.68	0.94	2.05	1.92	141.10	0.98
16-17.5-50-0.2	149.40	1.09	2.05	2.24	149.48	1.00
19-2.5-50-0.2	131.01	0.13	2.05	0.27	129.65	0.99
19-5-50-0.2	138.49	0.26	2.05	0.54	139.01	1.00
19-7.5-50-0.2	149.47	0.39	2.05	0.81	148.36	0.99
19-10-50-0.2	158.62	0.53	2.05	1.08	157.71	0.99
19-12.5-50-0.2	168.12	0.66	2.05	1.35	167.06	0.99
19-15-50-0.2	180.84	0.79	2.05	1.62	176.42	0.98
19-17.5-50-0.2	188.68	0.92	2.05	1.89	185.77	0.98
19-20-50-0.2	193.72	1.05	2.05	2.16	195.12	1.01
19-22.5-50-0.2	197.42	1.18	2.05	2.43	204.47	1.04
					Mean	1.00
					CoV	0.02

Table 16 Ultimate load comparison (Ring-0.3).

Specimen ID	$N_{u,Test(FE)}$	$\frac{t}{d}$	$\sqrt{\frac{f_{c,ring}}{f_c}}$	$\frac{t}{d}\sqrt{\frac{f_{c,ring}}{f_c}}$	$N_{u,Pred}$	$N_{u,Pred}/N_{u,Test(FE)}$
16-10-25-0.3-1	119.4	0.63	1.85	1.15	120.96	1.01
16-10-25-0.3-2	122.7	0.63	1.85	1.15	120.96	0.99

16-10-50-0.3-1	121.4	0.63	1.85	1.15	120.96	1.00
16-10-50-0.3-2	120.6	0.63	1.85	1.15	120.96	1.00
16-15-50-0.3-1	132.0	0.94	1.85	1.73	136.04	1.03
16-15-50-0.3-2	134.5	0.94	1.85	1.73	136.04	1.01
19-10-50-0.3-1	152.1	0.53	1.85	0.97	153.95	1.01
19-10-50-0.3-2	155.9	0.53	1.85	0.97	153.95	0.99
16-2.5-50-0.3	94.08	0.16	1.85	0.29	98.34	1.05
16-5-50-0.3	100.98	0.31	1.85	0.58	105.88	1.05
16-7.5-50-0.3	112.61	0.47	1.85	0.86	113.42	1.01
16-10-50-0.3	121.37	0.63	1.85	1.15	120.96	1.00
16-12.5-50-0.3	131.20	0.78	1.85	1.44	128.50	0.98
16-15-50-0.3	136.67	0.94	1.85	1.73	136.04	1.00
16-17.5-50-0.3	142.91	1.09	1.85	2.02	143.58	1.00
19-2.5-50-0.3	129.72	0.13	1.85	0.24	128.71	0.99
19-5-50-0.3	136.30	0.26	1.85	0.49	137.12	1.01
19-7.5-50-0.3	147.72	0.39	1.85	0.73	145.54	0.99
19-10-50-0.3	155.52	0.53	1.85	0.97	153.95	0.99
19-12.5-50-0.3	163.14	0.66	1.85	1.21	162.36	1.00
19-15-50-0.3	173.19	0.79	1.85	1.46	170.77	0.99
19-17.5-50-0.3	181.83	0.92	1.85	1.70	179.18	0.99
19-20-50-0.3	187.65	1.05	1.85	1.94	187.60	1.00
19-22.5-50-0.3	191.80	1.18	1.85	2.19	196.01	1.02
					Mean	1.00
					CoV	0.02

Table 17 Ultimate load comparison (Ring-0.4).

Specimen ID	$N_{u,Test(FE)}$	$\frac{t}{d}$	$\sqrt{\frac{f_{c,ring}}{f_c}}$	$\frac{t}{d}\sqrt{\frac{f_{c,ring}}{f_c}}$	$N_{u,Pred}$	$N_{u,Pred}/N_{u,Test(FE)}$
16-2.5-50-0.4	93.73	0.16	1.56	0.24	97.16	1.04
16-5-50-0.4	100.54	0.31	1.56	0.49	103.52	1.03
16-7.5-50-0.4	109.75	0.47	1.56	0.73	109.88	1.00
16-10-50-0.4	117.86	0.63	1.56	0.97	116.25	0.99
16-12.5-50-0.4	123.31	0.78	1.56	1.22	122.61	0.99
16-15-50-0.4	132.65	0.94	1.56	1.46	128.97	0.97
19-2.5-50-0.4	128.68	0.13	1.56	0.20	127.40	0.99
19-5-50-0.4	133.26	0.26	1.56	0.41	134.49	1.01
19-7.5-50-0.4	144.99	0.39	1.56	0.61	141.59	0.98
19-10-50-0.4	150.75	0.53	1.56	0.82	148.69	0.99
19-12.5-50-0.4	157.74	0.66	1.56	1.02	155.79	0.99
19-15-50-0.4	167.77	0.79	1.56	1.23	162.88	0.97
19-17.5-50-0.4	173.73	0.92	1.56	1.43	169.98	0.98
					Mean	0.99
					CoV	0.02

Table 18 Stress ratio comparison between FEA and analytical predictions (16 mm).

Model ID	λ_{FE}	λ_{Pred}	$\lambda_{Pred}/\lambda_{FE}$
16-2.5-50-0.2	0.534	0.556	1.04
16-5-50-0.2	0.362	0.350	0.97

16-7.5-50-0.2	0.246	0.240	0.98
16-10-50-0.2	0.161	0.173	1.08
16-12.5-50-0.2	0.125	0.131	1.05
16-15-50-0.2	0.100	0.102	1.02
16-17.5-50-0.2	0.082	0.082	1.00
16-20-50-0.2	0.065	0.067	1.02
16-2.5-50-0.3	0.542	0.556	1.03
16-5-50-0.3	0.356	0.350	0.99
16-7.5-50-0.3	0.245	0.240	0.98
16-10-50-0.3	0.165	0.173	1.05
16-12.5-50-0.3	0.128	0.131	1.03
16-15-50-0.3	0.102	0.102	1.00
16-17.5-50-0.3	0.083	0.082	0.99
16-20-50-0.3	0.067	0.067	1.00
16-2.5-50-0.4	0.550	0.556	1.01
16-5-50-0.4	0.375	0.350	0.93
16-7.5-50-0.4	0.259	0.240	0.93
16-10-50-0.4	0.174	0.173	1.00
16-12.5-50-0.4	0.137	0.131	0.96
16-15-50-0.4	0.107	0.102	0.95
16-17.5-50-0.4	0.085	0.082	0.97
16-20-50-0.4	0.071	0.067	0.93
		Mean	1.00
		CoV	0.04

Table 19 Stress ratio comparison between FEA and analytical predictions (19 mm).

Model ID	λ_{FE}	λ_{Pred}	$\lambda_{Pred}/\lambda_{FE}$
19-2.5-50-0.2	0.563	0.604	1.07
19-5-50-0.2	0.398	0.401	1.01
19-7.5-50-0.2	0.283	0.285	1.01
19-10-50-0.2	0.215	0.212	0.98
19-12.5-50-0.2	0.164	0.163	1.00
19-15-50-0.2	0.134	0.129	0.96
19-17.5-50-0.2	0.111	0.105	0.95
19-20-50-0.2	0.091	0.087	0.95
19-2.5-50-0.3	0.574	0.604	1.05
19-5-50-0.3	0.392	0.401	1.02
19-7.5-50-0.3	0.283	0.285	1.01
19-10-50-0.3	0.217	0.212	0.97
19-12.5-50-0.3	0.175	0.163	0.93
19-15-50-0.3	0.138	0.129	0.93
19-17.5-50-0.3	0.114	0.105	0.92
19-20-50-0.3	0.096	0.087	0.90
19-2.5-50-0.4	0.581	0.604	1.04
19-5-50-0.4	0.391	0.401	1.03
19-7.5-50-0.4	0.285	0.285	1.00
19-10-50-0.4	0.222	0.212	0.95
19-12.5-50-0.4	0.176	0.163	0.93
19-15-50-0.4	0.141	0.129	0.91

19-17.5-50-0.4	0.117	0.105	0.90
19-20-50-0.4	0.099	0.087	0.87
		Mean	0.97
		CoV	0.05

Figures

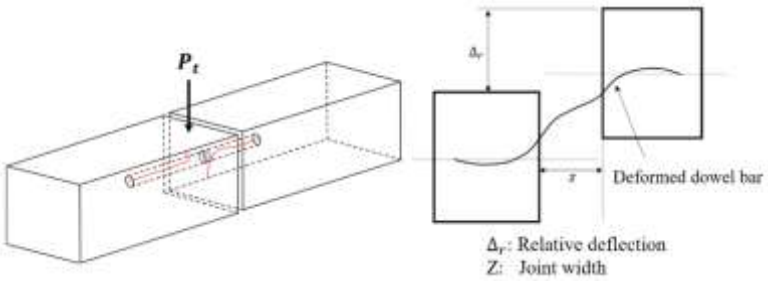

(a)

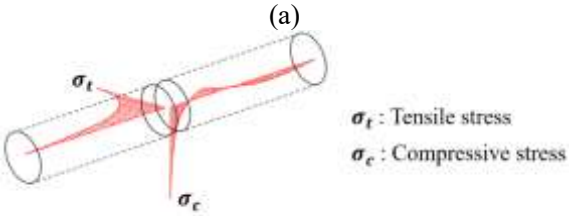

Stress distribution in dowel slot

(b)

Figure 1. Dowel bar load transfer mechanism (Guo and Chan 2022a).

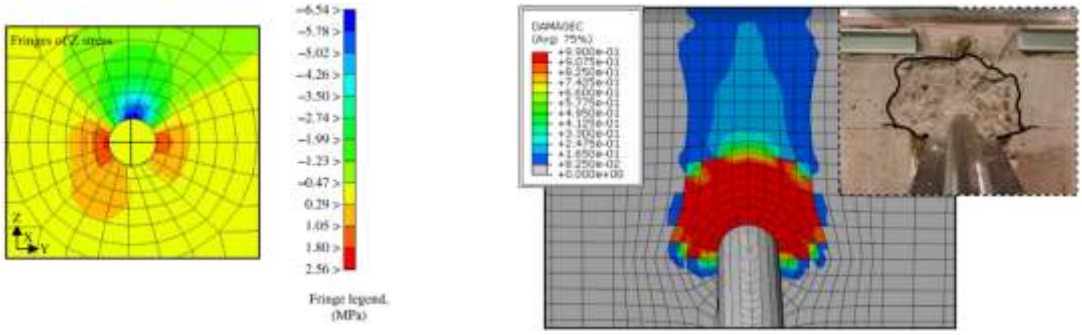

(a) (b)

Figure 2. Surface-to-surface contact modelled compressive stress concentration and concrete crushing, (a) compressive stress concentration (Riad et al. 2009), (b) concrete crushing (Guo and Chan 2022c).

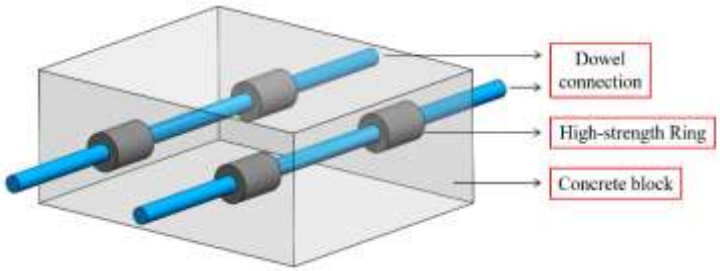

Figure 3. Configuration of the high-strength ring strengthened dowel connection (Guo et al. 2023).

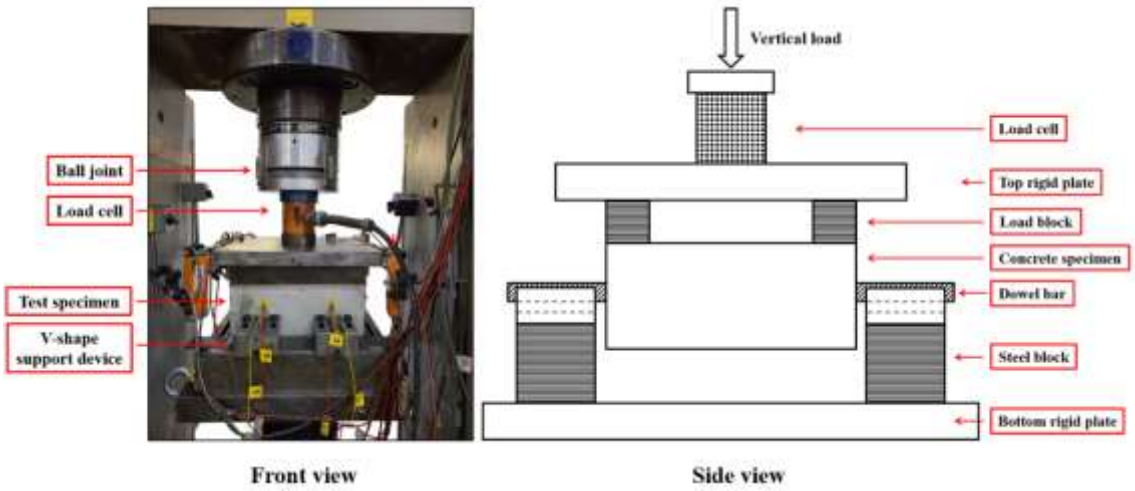

Figure 4. Test setup of the high-strength ring strengthened dowel connection embedded into concrete (Guo et al. 2023).

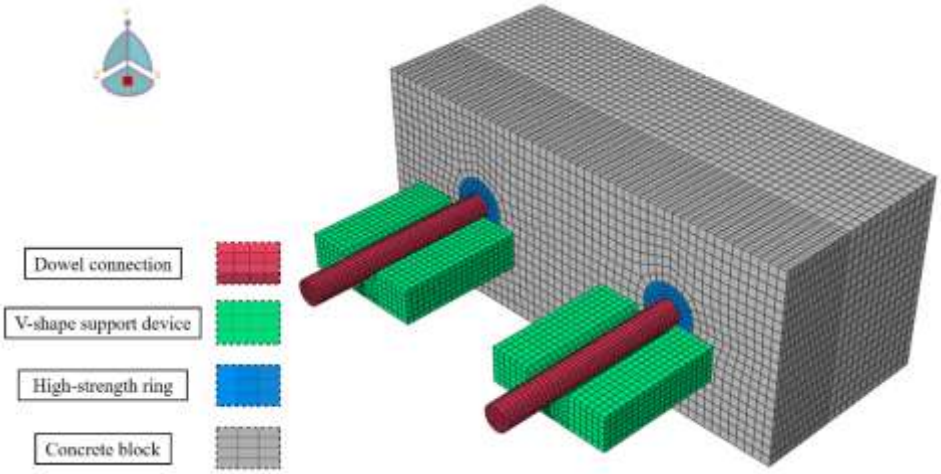

(a)

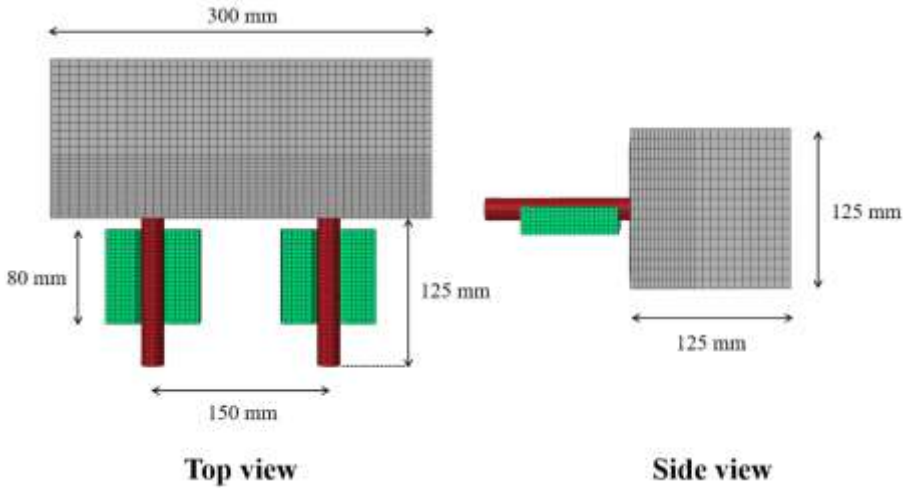

(b)

Figure 5. Finite element model (a) configuration, (b) model dimension.

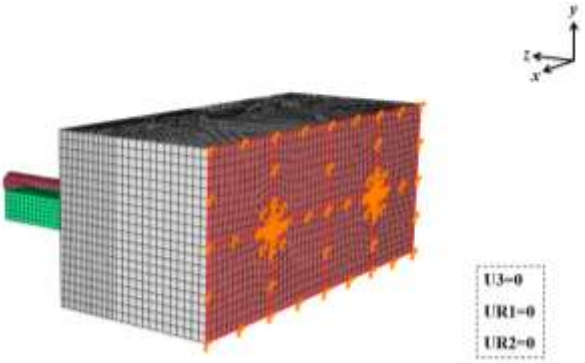

(a)

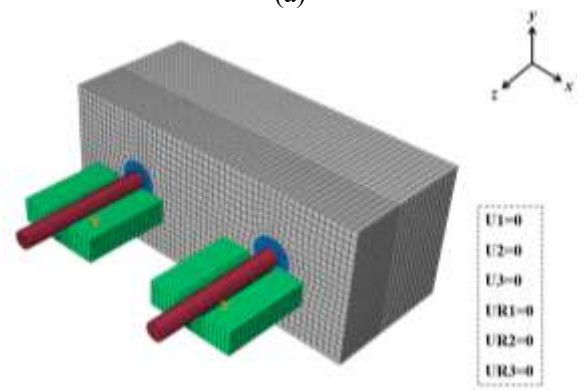

(b)

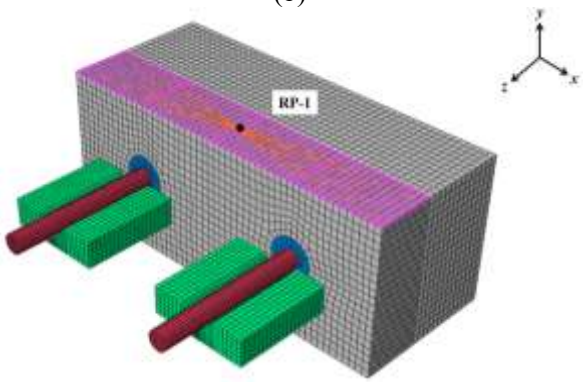

(c)

Figure 6. Boundary conditions and load arrangement (a) symmetric constraint, (b) fixed constraint, (c) load arrangement.

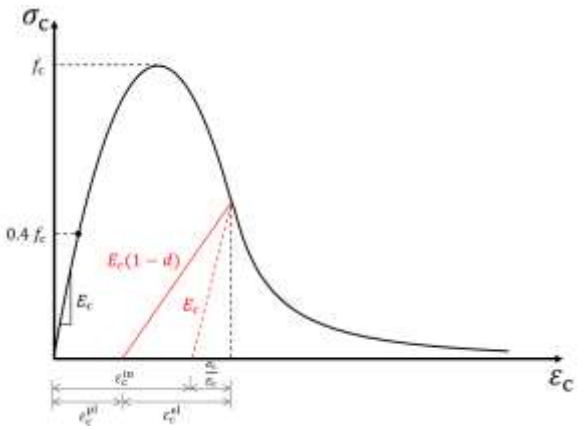

Figure 7. Concrete damage variable definition.

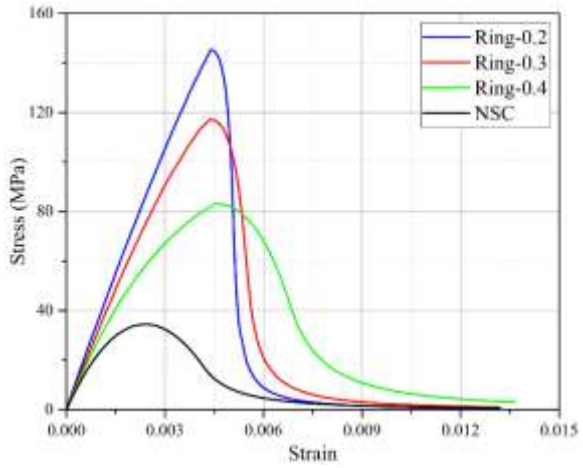

Figure 8. Compressive stress-strain relationships of normal-strength concrete (NSC) and high-strength concrete (HSC).

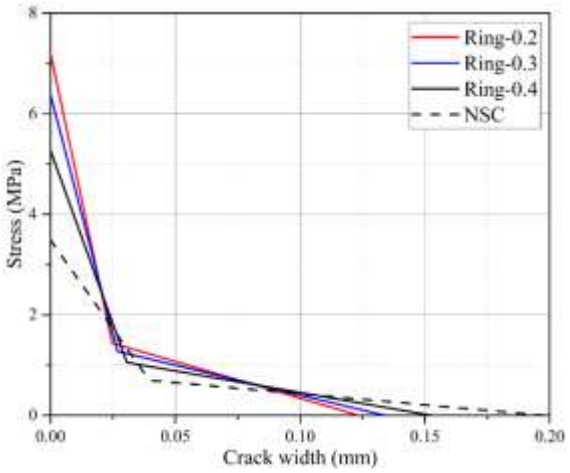

Figure 9. Tensile stress-crack width relationships of NSC and HSC.

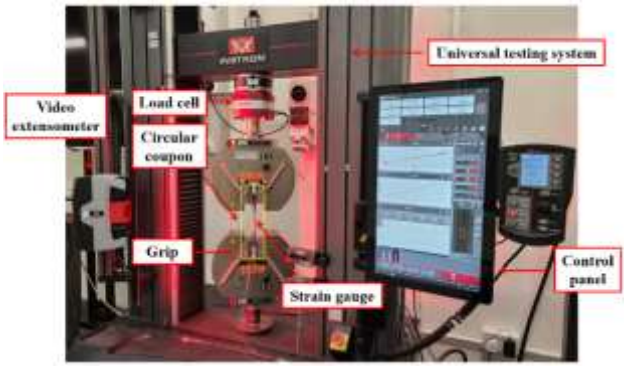

(a)

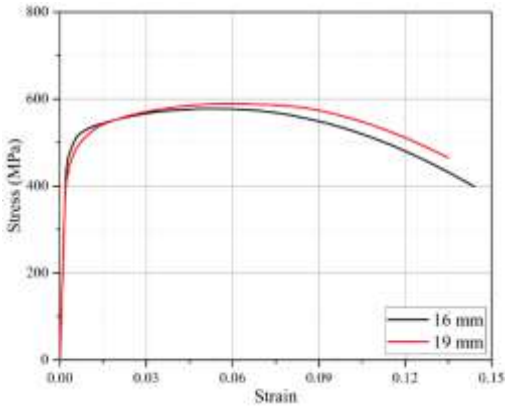

(b)

Figure 10. Uniaxial tension test and stress-strain relationship of dowel connections (a) uniaxial tension test, (b) stress-strain curves (Guo et al. 2023).

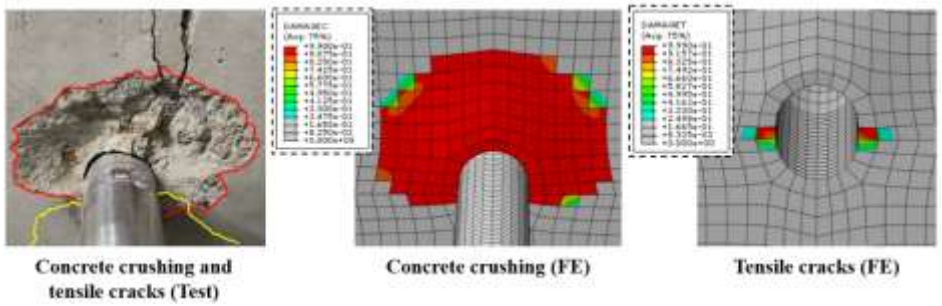

(a)

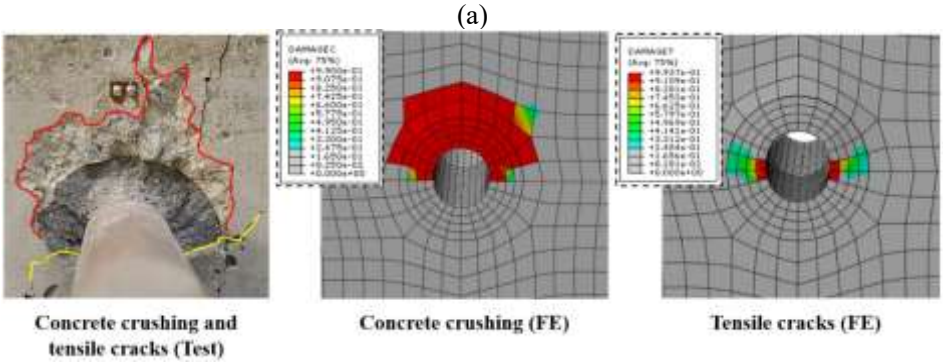

(b)

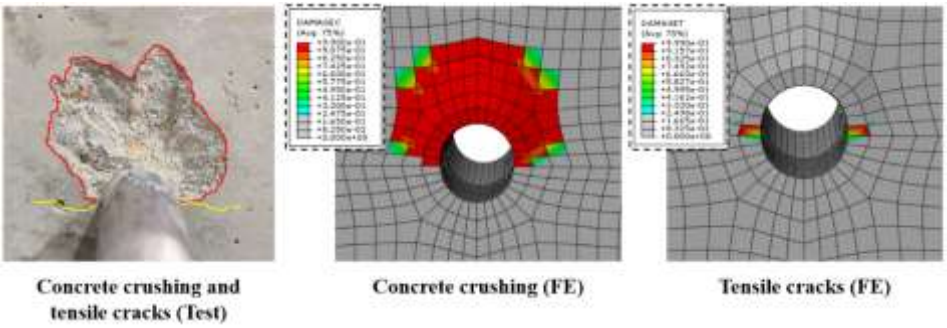

(c)

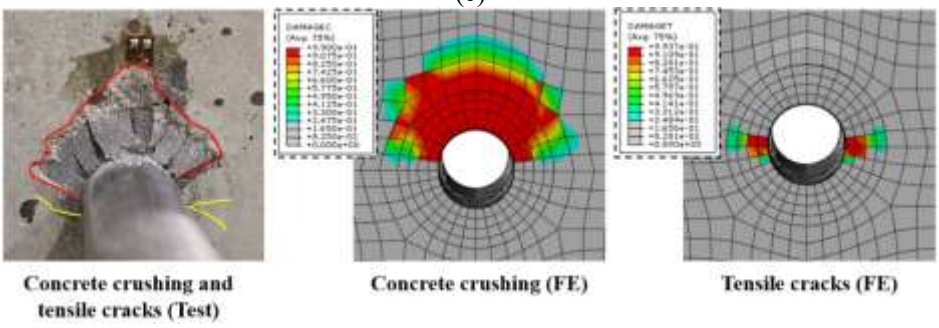

(d)

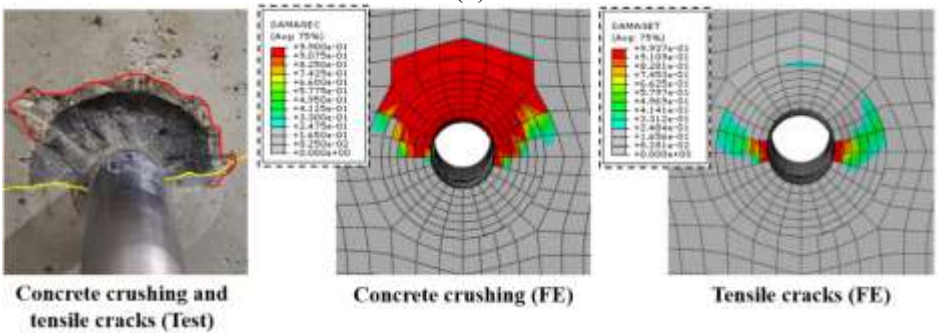

(e)

Figure 11. Concrete crushing and tensile cracks from tests and finite element analysis (FEA) (a) 16 mm, (b) 16-10-50-0.3, (c) 19 mm, (d) 19-10-50-0.3, (e) 19-15-50-0.2.

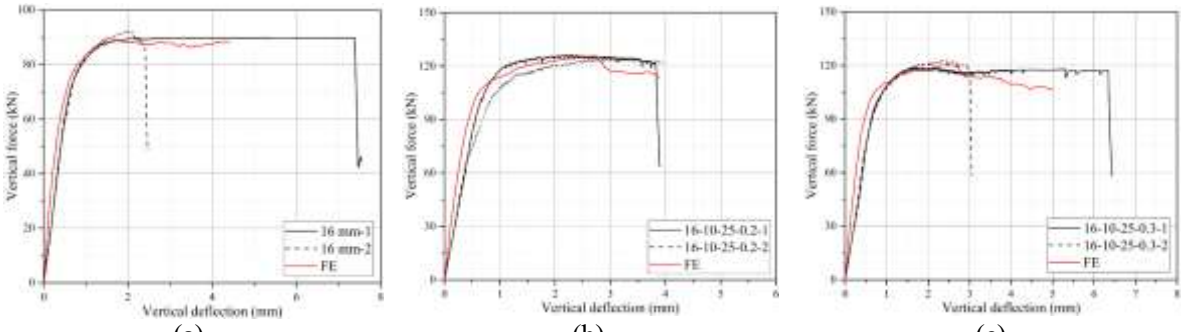

(a) (b) (c)

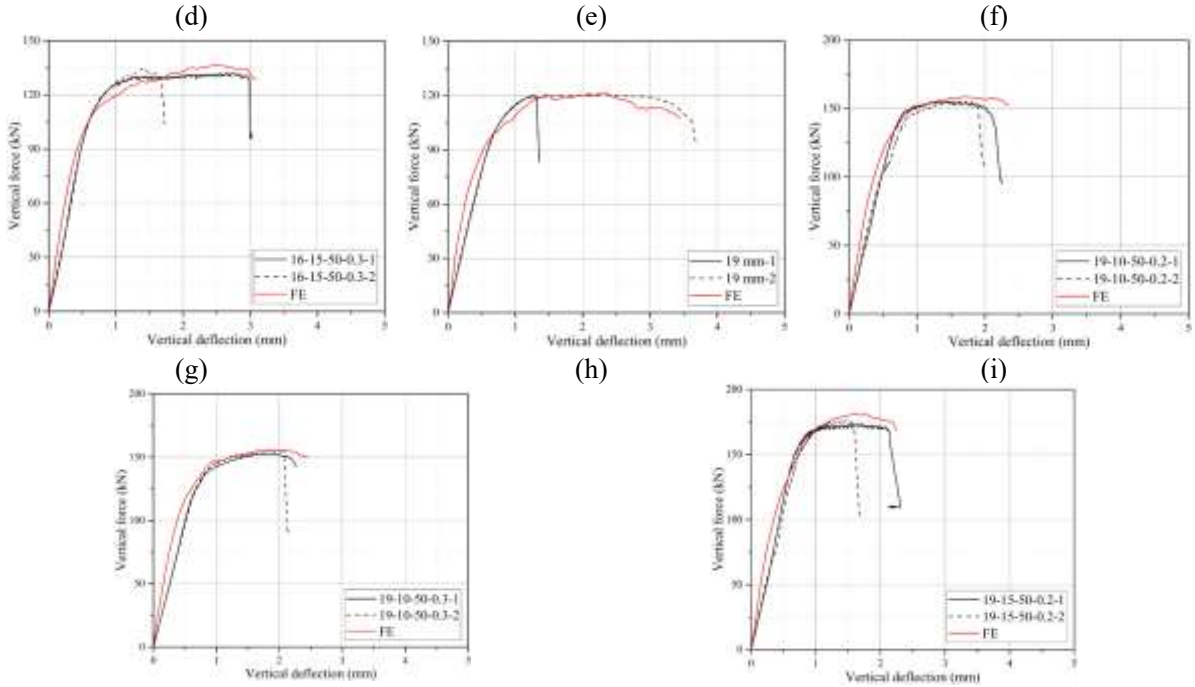

Figure 12. Load-deflection relationships from tests and FEA (a) 16 mm, (b) 16-10-25-0.2, (c) 16-10-25-0.3, (d) 16-10-50-0.2, (e) 16-10-50-0.3, (f) 16-15-50-0.2, (g) 16-15-50-0.3, (h) 19 mm, (i) 19-10-50-0.2, (j) 19-10-50-0.3, (k) 19-15-50-0.2

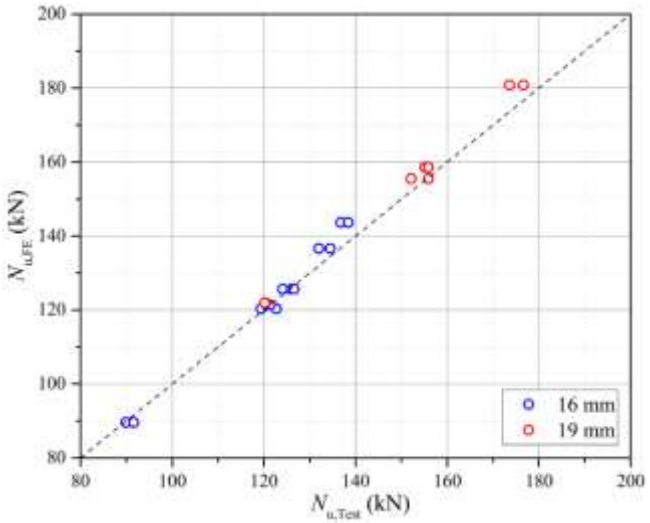

Figure 13. Ultimate loads from tests and FEA.

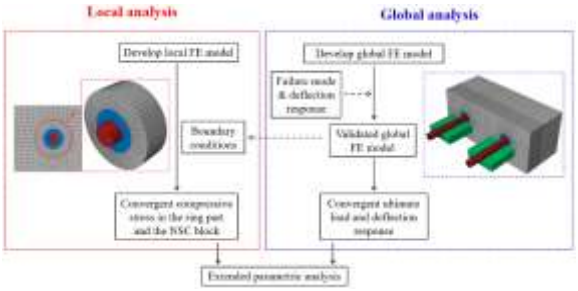

Figure 14. The global-local FEA in ABAQUS.

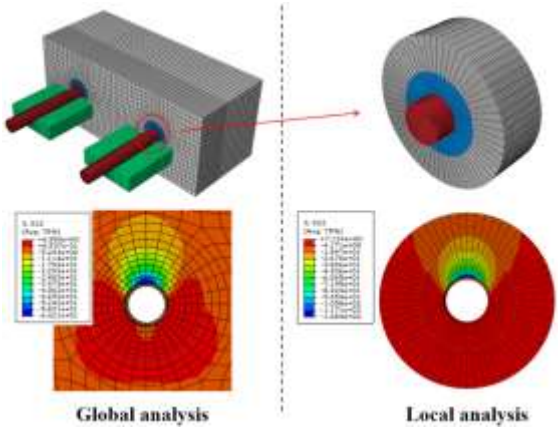

Figure 15. Compressive stress prediction in global-local analysis (19-10-50-0.2).

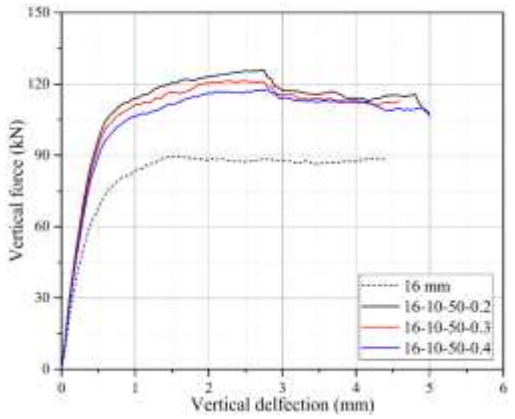

(a)

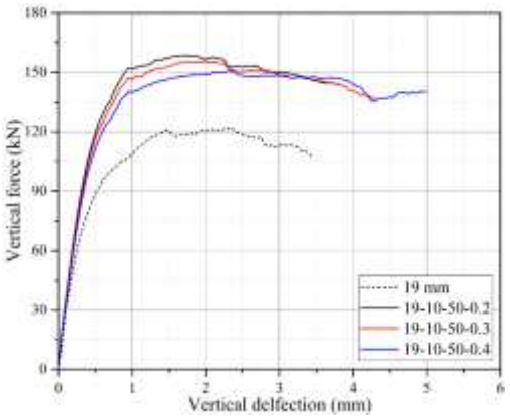

(b)

Figure 16. Deflection responses with different types of high-strength rings.

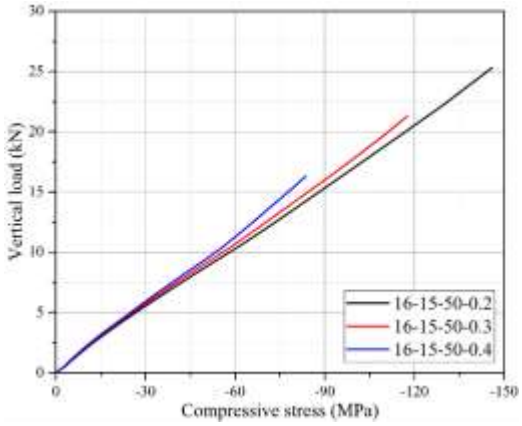

(a)

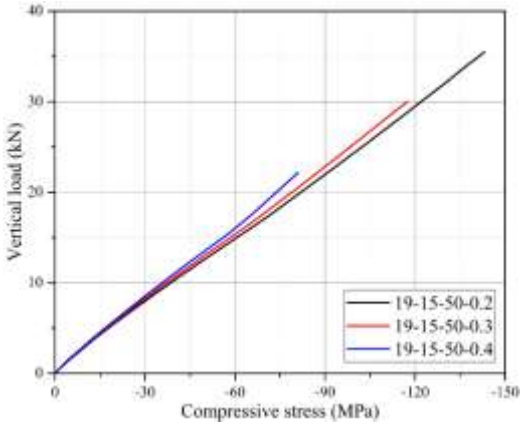

(b)

Figure 17. Compressive stress development of HSC.

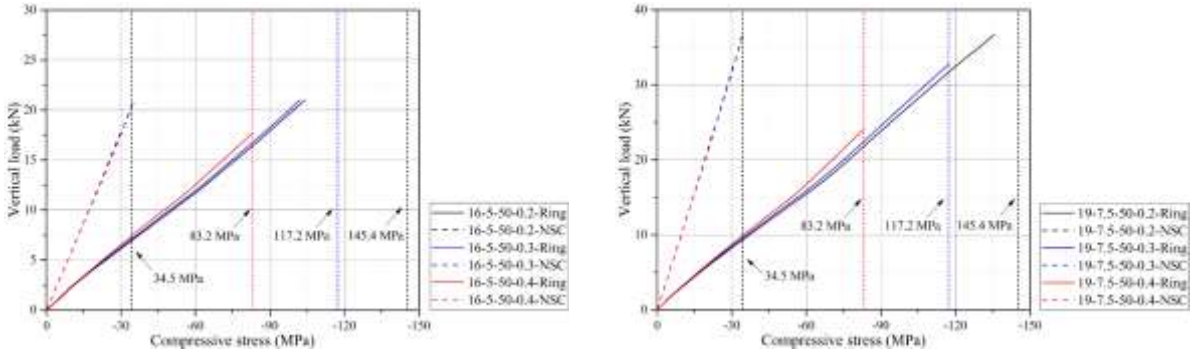

(a) (b)

Figure 18. Compressive stress developments of HSC and NSC.

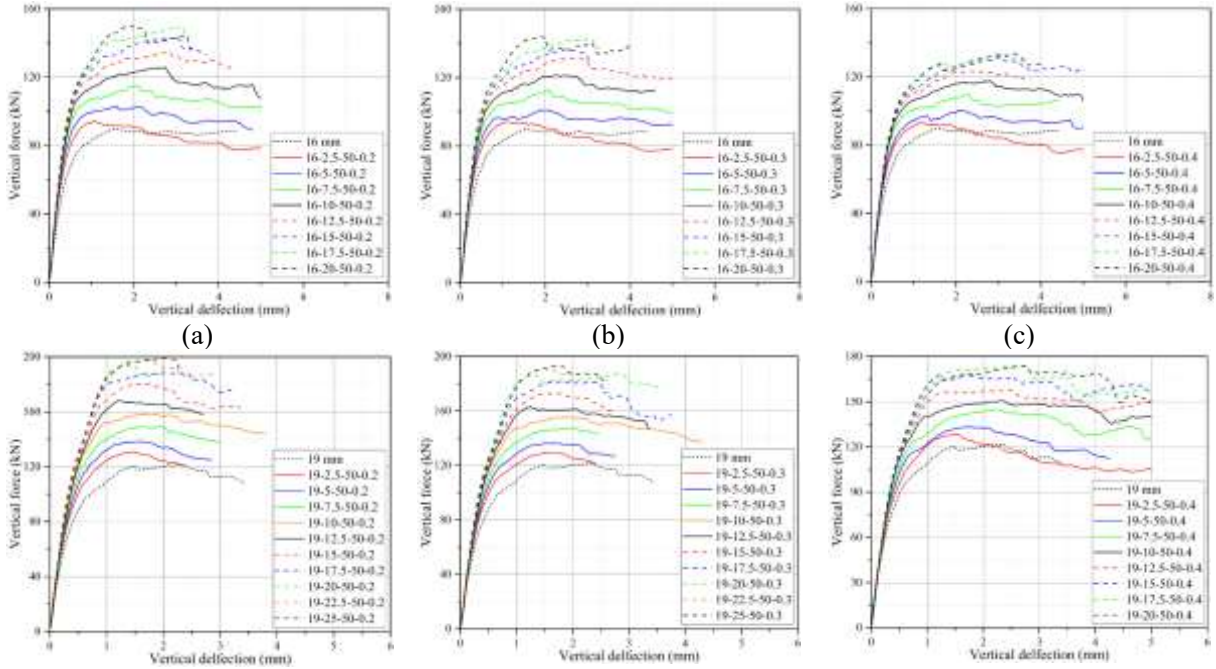

(a) (b) (c)

(d) (e) (f)

Figure 19. Load-deflection relationships of models with high-strength rings of different thicknesses (a) 16 mm-0.2, (b) 16 mm-0.3, (c) 16 mm-0.4, (d) 19 mm-0.2, (e) 19 mm-0.3, (f) 19 mm-0.4.

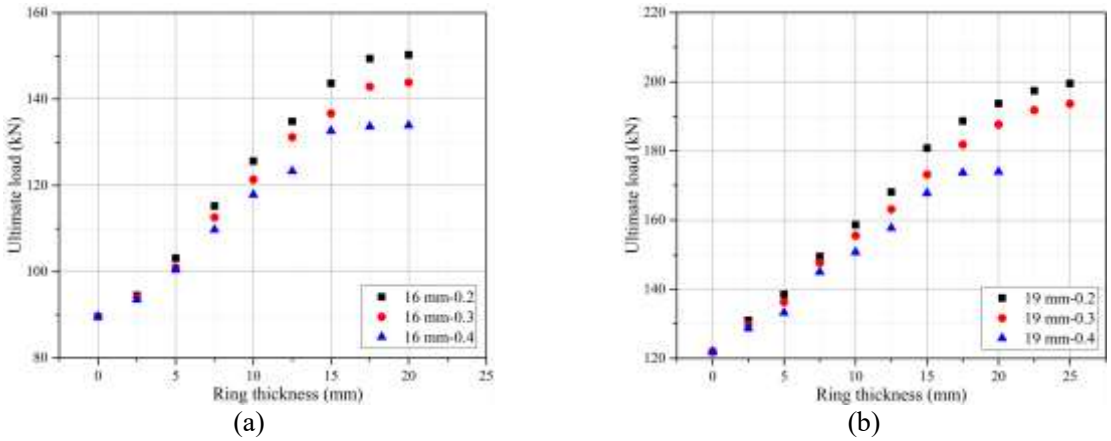

(a) (b)

Figure 20. Relationship between ultimate load and high-strength ring thickness (a) 16 mm, (b) 19 mm.

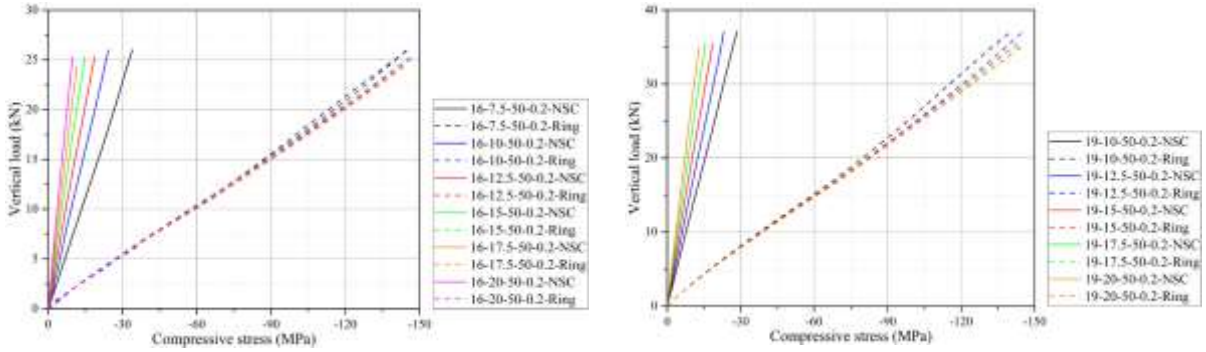

(a) (b)

Figure 21. Compressive stress development in high-strength ring and NSC block (a) 16 mm-0.2, (b) 19 mm-0.2.

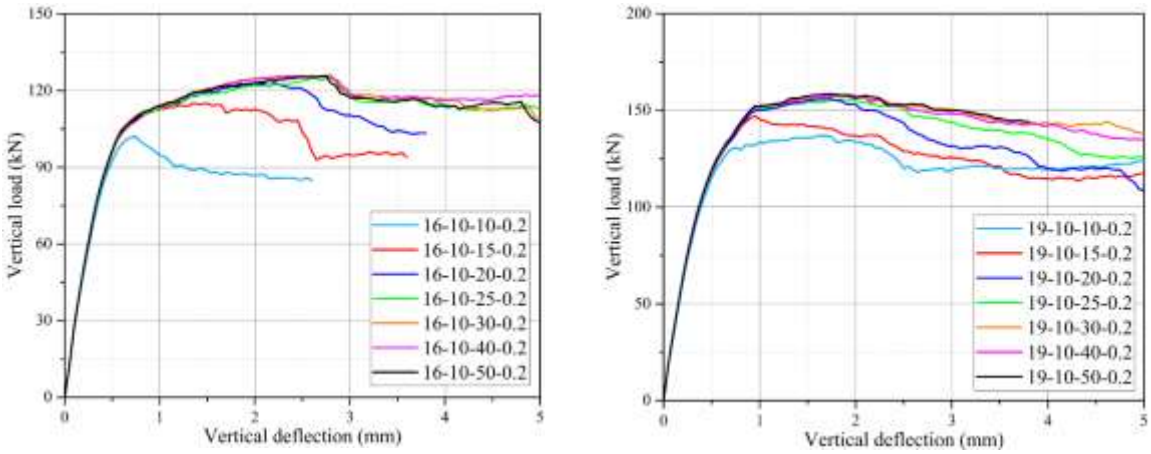

(a) (b)

Figure 22. Load-deflection curves of models strengthened by high-strength rings of different lengths (a) 16 mm-0.2, (b) 19 mm-0.2.

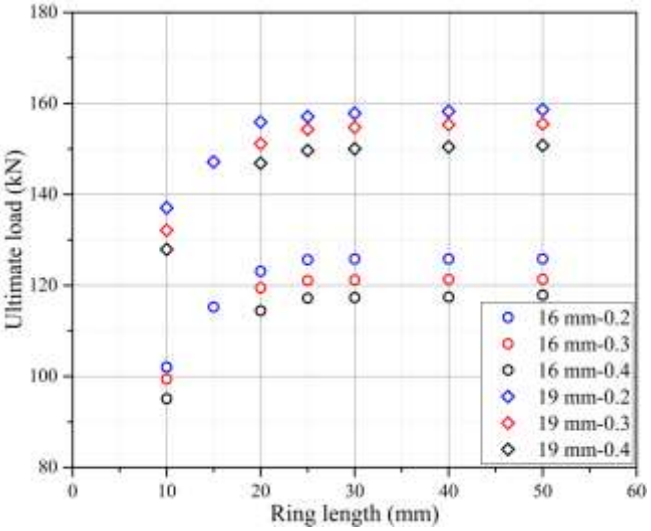

Figure 23. Relationship between ultimate load and high-strength ring length (high-strength ring thickness: 10 mm).

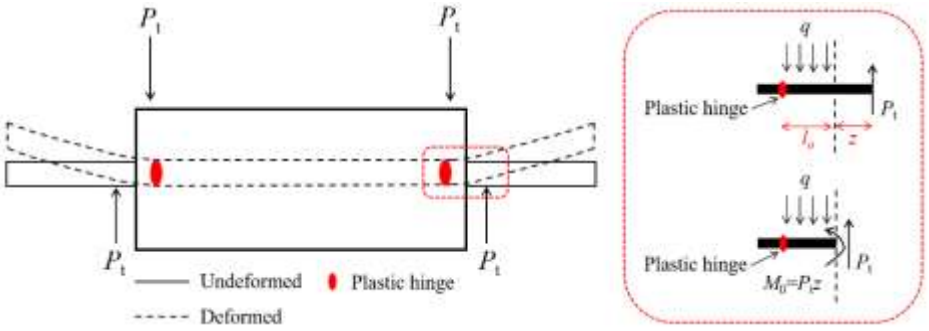

Figure 24. Force diagram of dowel connection embedded into concrete (Guo et al. 2023).

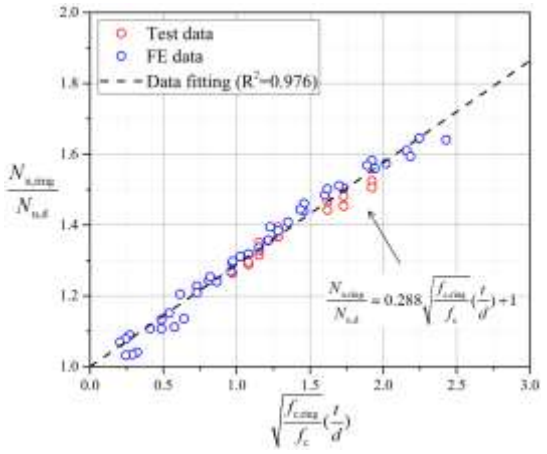

Figure 25. Ultimate load prediction.

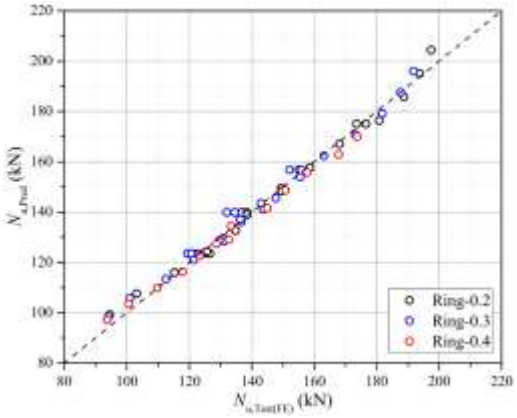

Figure 26. Ultimate load comparison.

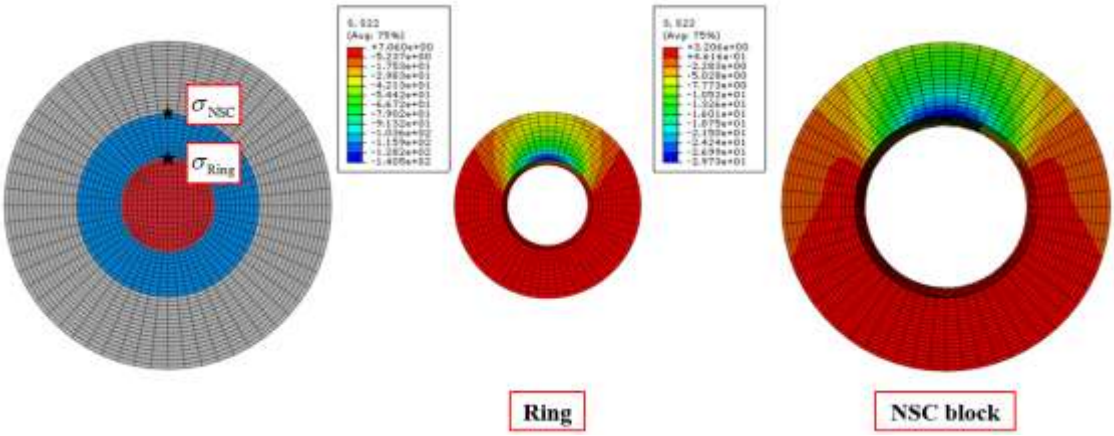

Figure 27. Maximum compressive stress generated in local FEA.

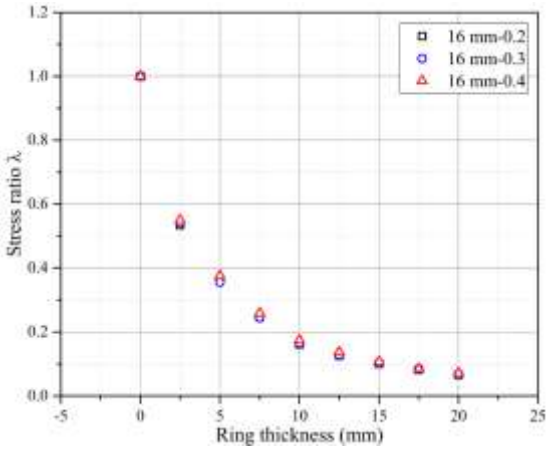

(a)

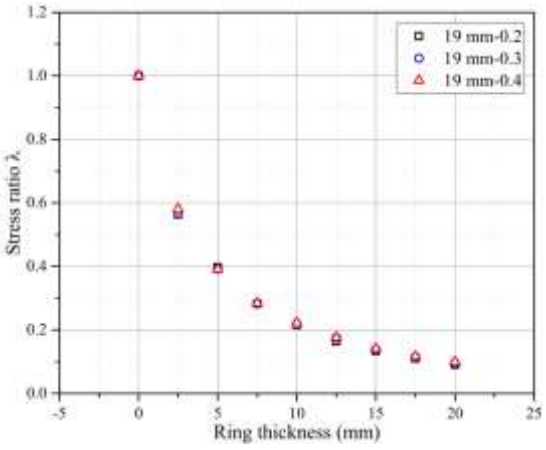

(b)

Figure 28. Relationship between stress ratio and ring thickness (a) 16 mm, (b) 19 mm.

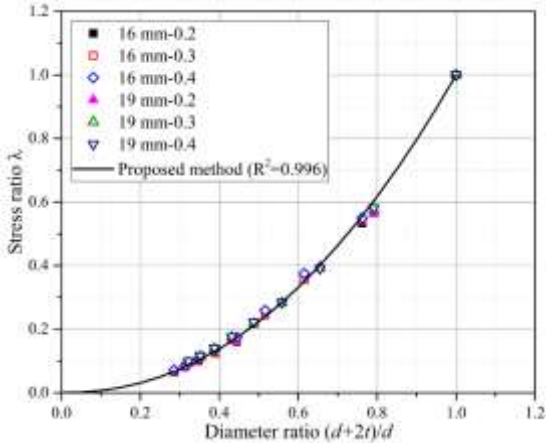

Figure 29. Relationship between stress ratio and diameter ratio.

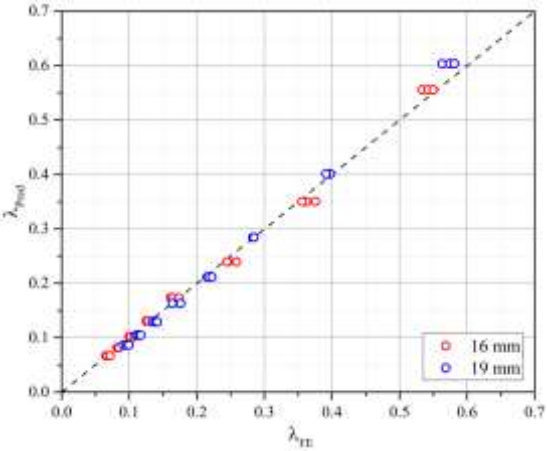

Figure 30. Stress ratio comparison between FEA and analytical prediction.